Can the Rate of a Catalytic Turnover be Altered by Ligands in the Absence of Direct Binding Interactions?

Jacklyn N. Hall[1†], Stephen P. Vicchio[2], A. Jeremy Kropf[3], Massimiliano Delferro[3], and Praveen Bollini[1,*]

1. William A. Brookshire Department of Chemical and Biomolecular Engineering; University of Houston; Houston, TX 77204, USA

2. Department of Chemical and Biomolecular Engineering, Clemson University, Clemson, SC 29634

3. Chemical Sciences and Engineering Division, Argonne National Laboratory, Lemont, IL 60439, USA

KEYWORDS metal-organic frameworks, second sphere effects, oxidation catalysis

ABSTRACT: Second sphere coordination effects ubiquitous in enzymatic catalysis occur through direct interactions – either covalent or non-covalent – with reaction intermediates and transition states. We present herein evidence of *indirect* second sphere coordination effects in which ligation far removed from the primary coordination sphere of the active site nevertheless alters energetic landscapes within catalytic redox cycles in the *absence* of direct physicochemical interactions with surface species mediating catalytic turnovers. Density functional theory, in-situ X-ray absorption and infrared spectroscopy, and a wide array of steady state and transient data suggest that the presence of peripheral water renders oxidation half cycles within two-electron redox cycles over μ_3-oxo bridged trimers in MIL-100(M) more kinetically demanding. Communication between ligated water and the active site appears to occur through the Fe-O-Fe backbone as inferred from spin density variations on the central μ_3-oxygen 'junction'. Evidence is provided for the generality of these second sphere effects in that they influence different types of half cycles or metals, and can be amplified or attenuated through a judicious choice of coordinating ligand. Specifically in the case of MIL-100(M) materials, the Cr isostructure can be made to kinetically mimic the Fe one by disproportionately hindering the oxidation half cycle relative to the reduction half cycle. Results and inferences presented significantly expand both the conceptual definition of second sphere effects, as well as the palette of synthetic levers available for tuning catalytic redox performance through chemical ligation.

1. Introduction

Metal-organic framework (MOF) materials provide a platform for hosting and subjecting to kinetic and spectroscopic investigation well-defined active site moieties the catalytic properties of which may be challenging to discern over materials less uniform in nature. They serve as platforms for polymetal oxo clusters that are a ubiquitous, key feature of biological systems including ribonucleotide reductase, purple acid phosphatases, and methane monooxygenases. Although the nature of the precise chemical and biological function of these clusters has attracted significant interest from the bioinorganic chemistry community,[1–3] their systematic kinetic investigation remains hampered by the tendency for polynuclear aggregation exhibited by homogeneous complexes on the one hand,[4] and the distribution in nuclearity and coordination environment that limits unambiguous quantitative inquiry into metal-zeolites and oxides on the other.[5] MOFs, as hosts of highly uniform and well-defined oxo clusters, offer an opportunity for elucidating, with clarity, the precise relationship between the coordination environment of these clusters and their catalytic function.

More specifically, MIL-100 – a MOF carrying trinuclear μ_3-oxo nodes (Figure 1) – has been investigated heavily in this regard, with its uniformity from a structural,[6] adsorptive,[7–9] and reactive[10,11] standpoint having been evidenced abundantly in the open literature. Oxo-bridged trimer complexes of the

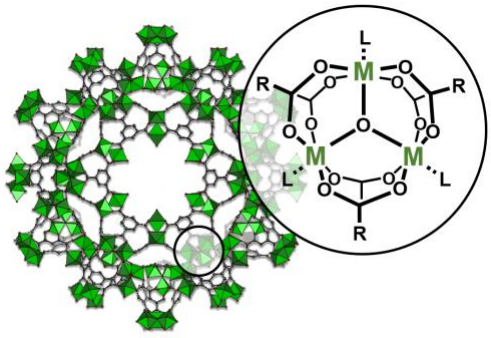

Figure 1. Schematic representation of trinuclear μ_3-oxo metallic complexes carrying the general formula

$[M_3O(O_2CR)_6(L_3)]^{n+}$ hosted within and the structure of metal-organic framework MIL-100. Adapted from Ref. [12], Copyright 2018 WILEY-VCH Verlag GmbH &Co. KGaA, Weinheim.

type hosted by MIL-100(M) materials have been the focus of intensive study[13–15] due to their rich magnetic[16–19] and electronic properties.[20–24] They also appear to be highly fungible from a structural perspective and exceedingly promiscuous from a catalytic perspective, with homogeneous complexes having been synthesized in a variety of transition metal compositions,[14,15,20,25,26] and demonstrated to catalyze, among others, epoxidation, oxidation, and hydrogenation reactions.[20,27–29]

Second sphere effects in which the coordination environment external to the immediate coordination sphere of the active site influence rates and selectivity are known to play a determinative role in metalloenzyme catalysis.[30,31] These second sphere effects can include spatial constrainment/confinement[32] and non-covalent interactions between ligands and reaction intermediates/transition states.[33] Both these effects manifest as direct interactions – either binding interactions that stabilize reaction intermediates and transition states, or non-binding ones that constrain or confine these reactive species. The common thread connecting these various interactions is the alteration of physicochemical characteristics of molecules, intermediates, and transition states that the secondary sphere atoms are *directly* in chemical or physical contact with. We report here what is to the best of our knowledge a unique manifestation of second sphere coordination effects in which ligands present on an oxo-bridged trimer alter the stability of kinetically relevant oxo-formation and scavenging transition states *without* direct interactions with molecular species involved in the effectuation of catalytic turnovers. Two-electron redox cycles occurring over highly uniform MIL-100(M) nodes are subjected to kinetic, spectroscopic, and DFT analysis to reveal ligand effects on reactivity that seem to occur through communication by means of the μ-oxo bridge connecting the cluster metal atoms rather than (non)-covalent interactions with reaction intermediates and transition states. The generality of these effects is demonstrated through application to multiple MIL-100 isostructures, contrasting redox half cycles, and a range of oxygenate ligands.

2. Materials and Methods

2.1. MIL-100 Synthesis and Characterization. Synthesis and characterization protocols used for the MIL-100(Fe) and MIL-100(Cr) samples used herein are described in detail in previously published works.[10,11] N_2 physisorption, X-ray diffraction (XRD), and thermogravimetric analysis (TGA) measurements were used in these works to evaluate sample porosity, crystallinity, and chemical composition, respectively.

2.2.CO Oxidation Experiments. Kinetic measurements for CO oxidation with N_2O were conducted using procedures described in a preceding publication.[34] Briefly, catalyst samples were treated under inert flow (50 cm^3 min^{-1} He, Matheson, Ultra High Purity) or vacuum (P < 0.01 kPa, Pfeiffer Pascal 2005 SD rotary vane vacuum pump) for 12 hours at 423 – 548 K prior to reaction. Product and reactant concentrations were monitored using either a gas chromatograph (Agilent 7890 B, HP-PLOT-Q capillary column (30 m x 320 μm x 0.2 μm) with a thermal conductivity detector) or an online mass spectrometer (MKS Cirrus 2) depending on the nature of the experiment.

2.3. In-Situ Active Site Titrations. In-situ titrations with NO were carried out using procedures similar to those detailed in a preceding study using either 1000 ppm NO/N_2 or 10% NO/N_2 (Matheson, Research Grade) two-component gas mixtures of NO.[34] For titrations involving H_2O and for H_2O co-feed experiments, a syringe pump (KD Scientific, Model 100) was used to introduce H_2O (deionized, 18.3 MΩ), with gas lines maintained at 383 K to avoid condensation. In the case of either titrant, reported coverages or quantities adsorbed were determined by measuring the breakthrough curve for the adsorbate with respect to an internal standard (either Ar or N_2) using a mass spectrometer at the reactor outlet.

2.4. Infrared Spectroscopy Measurements. Detailed procedures for transmission infrared spectroscopy measurements conducted here are reported in a preceding publication.[34] Following thermal activation under a given condition (423 – 548 K, inert flow or vacuum), spectra of the sample at the analysis temperature were used as background for NO/H_2O titration experiments. Spectra for a given analysis were collected on the same sample wafer and reported without normalization. Baseline corrections and peak integrations were completed using Origin 8.5.

2.5. In-Situ X-ray Absorption Spectroscopy Analysis. X-ray absorption fine structure (XAFS) spectroscopy experiments were conducted at Argonne National Laboratory, Advance Photon Source (APS) 10-BM beamline. Spectra at the Fe K-edges were collected in transmission mode with simultaneous measurement of the metal foil spectra for use in energy calibrations, with the inflection point taken as 7110.75 eV.[35] The *Demeter/Athena/Artemis* suite of XAFS analysis software[36] was used for data processing. Detailed descriptions of the microreactor flow cell used for in-situ spectroscopy measurements of MIL-100 are provided in a previous publication.[34] Crystallographic information files for MIL-100(Fe)[37] were used to consider the local structure of the catalyst node when fitting EXAFS spectra; scattering paths were calculated using *feff* version 6.[38]

XAFS spectra of the as-synthesized sample was initially collected at room temperature under a 10 mL min^{-1} He flow. The materials were then treated for a minimum of 1 hour at 523 K, after which the spectra of the thermally activated sample was obtained (523 K). The samples were subsequently cooled to 313 K to obtain spectra near room temperature for a more direct comparison to the as-synthesized samples when analyzing EXAFS fitting results related to changes in the local coordination environment of the trimer nodes. Single scattering M-O (first shell, N = 5-6) scattering paths were considered during analysis.

2.6. Coordinated Ligand Exchange and Quantification. The following procedure was employed in order to produce MIL-100(Fe) catalyst samples with targeted quantities of coordinated alkanol (methanol, ethanol, and isopropanol) ligands. First, MIL-100(Fe) was thermally activated at 523 K for 12 hours under He flow to remove a majority of the

coordinated water and hydroxide species. The sample was then exposed to 0.2 kPa of the desired alcohol under He flow at 373 K in order to create a catalyst surface containing predominantly coordinated alcohol and alkoxide species. Next, the samples were purged overnight at temperatures between 423 and 448 K to allow sufficient time for removal of gaseous alkanol species and elimination of a fraction of the coordinated ligands from the surface. After purging between 423 and 448 K, the catalyst sample was evaluated for the oxidation of CO with N_2O and the steady-state rate determined. After reaction, the quantity of Fe^{2+} open-metal sites available was determined by in-situ titration with NO. Following this, D_2O adsorption experiments were conducted to quantify the density of coordinated alkanol ligands. As evaluated in our previous work,[11] under standard conditions, the introduction of D_2O vapor over MIL-100(Fe) reveals the evolution of both H_2O and HDO from the catalyst surface, related to the replacement of coordinated H_2O with D_2O ($Fe^{3+}\cdots H_2O + D_2O_{(g)} \leftrightarrow Fe^{3+}\cdots D_2O + H_2O_{(g)}$) and reaction between D_2O and hydroxides ($Fe^{3+}\cdots OH^- + D_2O_{(g)} \leftrightarrow Fe^{3+}\cdots OD^- + HDO_{(g)}$), respectively. As shown previously,[11] cumulative moles of H_2O and HDO formed can serve as proxies for the density of coordinated water ($Fe^{3+}\cdots H_2O$) and hydroxides ($Fe^{3+}\cdots OH^-$), and be used to estimate the corresponding Fe^{3+} and Fe^{2+} open-metal site densities. Here, an identical methodology was employed to quantify the density of the coordinated alkanol of interest and to subsequently determine the alkanol to Fe_3O molar ratio at each condition (Section S2.1, Supporting Information) as the use of D_2O allows us to differentiate between coordinated alkanols and alkoxides. Due to the lack of calibration data for deuterated alcohols (specifically C_2H_5OD and $(CH_3)_2CHOD$), Fe^{2+} open-metal site densities were estimated solely from NO titration data, and not from the quantity of deuterated alkanol evolved during D_2O adsorption experiments.

2.7. Quantum Chemical Calculations. Quantum chemical calculations, specifically Density Functional Theory (DFT), were used to elucidate geometric and electronic phenomena associated with N_2O activation on MIL-100(Fe) nodes varying in H_2O content. The unrestricted M06-L functional[39] with def2-TZVP basis sets[40,41] was implemented in *Gaussian 16*.[42] Following prior work, this level of theory is adequate to capture the electronic structure of MIL-100(Fe) inorganic nodes, as discussed extensively elsewhere by Vitillo et al.[43–45] The initial MIL-100(Fe) structures were selected from Vitillo et al.,[43] with variations in the water content simulated by adding coordinated H_2O ligands to MIL-100 Fe(III) sites. Trimers with three distinct degrees of hydration were considered: no H_2O ligands coordinated to the trimer, an H_2O ligand coordinated to one of two Fe(III) sites in the trimer, and an H_2O ligand coordinated to each of the two distinct Fe(III) sites present in the trimer. We refer to these three trimers using the following notation: Fe_3O – 0 H_2O, Fe_3O – 1 H_2O, and Fe_3O – 2 H_2O. Structural and sample input files are reported in the SI as well as GitHub.[46] Sample calculation files can be found in Section S1.1 of the SI.

Enthalpies were estimated at standard conditions (1 atm and 25 °C) using vibrational modes calculated from *Gaussian 16*. All vibrational modes below 50 cm^{-1} were replaced with 50 cm^{-1} while calculating vibrational partition functions following prior work.[47] Using the pMuTT python package, the vibrational partition functions were computed to determine the enthalpic vibrational contribution.[48] The electronic, translational, and rotational contributions were derived from Gaussian. Additionally, all reported energies were corrected for basis set supposition error (BSSE), as implemented directly in *Gaussian 16*. S1.2 Basis Set Superposition Error Fragment Information in the SI discusses how the BSSE error term was computed. Additionally, broken symmetry calculations were conducted using *Gaussian 16* to assign different alpha and beta spins on the Fe(III) sites (see SI S1.3).

3. Results and Discussion

3.1. Mechanism for CO oxidation over MIL-100(Fe). Quantitative analysis of steady state, transient stoichiometric, and isotopic tracer experiments suggest that CO oxidation with N_2O over divalent sites in MIL-100(Fe) occurs through a sequential mechanism comprised of distinct oxidation and reduction half cycle steps conjoined by an active oxygen intermediate.[34] These data can be rationalized using the sequence of elementary steps depicted in Scheme 1 involving 1) quasiequilibrated adsorption of N_2O onto Fe^{2+} sites, 2) irreversible formation of the active oxygen intermediate through N-O bond scission, 3) reversible adsorption of CO onto the active oxygen intermediate, 4) irreversible M-O bond scission to form bound CO_2, and 5) quasiequilibrated desorption of CO_2 into the gas phase. This partition between oxidation and reduction half cycle steps allows for the estimation of lumped kinetic parameters characterizing solely either oxidation half cycles (in which metal-oxygen bonds are formed), or reduction half cycles (in which metal-oxygen bonds are cleaved). A similar mechanism appears to mediate CO oxidation over MIL-100(Cr), but with more energetically demanding reduction half cycle steps that become kinetically relevant at much lower N_2O:CO ratios than MIL-100(Fe). No indications of site non-uniformity in samples activated at 523 K devoid of bound water and hydroxyls were identified during in-situ titrations with NO at a single titrant pressure in which fractional oxidation rates decrease linearly with equilibrium coverage of Fe^{2+}-nitrosyls, suggesting that every Fe^{2+} site present on a fully activated MIL-100(Fe) sample turns over at an identical rate. The uniformity of Fe^{2+} sites on fully activated MIL-100 samples are further reinforced by the close correspondence between cumulative methanol yields obtained during stoichiometric oxidation of methane with N_2O, and theoretical maximum Fe^{2+} open-metal site densities prevalent under reaction conditions.[10] Next, we probe whether this uniformity *also* extends to CO oxidation over Fe^{2+} sites present on partially activated MIL-100 beds with trimers carrying hydroxyl and water ligands.

3.2. Turnover rates over partially activated MIL-100(Fe) beds. Partially activated MIL-100(Fe) samples containing intermediate densities of bound waters and hydroxyls were generated by subjecting beds to varying thermal treatment temperatures. NO breakthrough-derived Fe^{2+} site densities increase monotonically with treatment

temperature (Figure 2a),[10] consistent with previous reports that use comparable thermal treatment protocols to elucidate adsorptive properties of Fe^{2+} sites.[49] Surprisingly, turnover rates per Fe^{2+} site were also found to increase monotonically with treatment temperature despite the uniform nature of the sample under consideration (Figure 2a). These variations in turnover rate are not attributable to changes in catalyst structure or composition given the combination of XRD, N_2 physisorption, and TGA data that evidence minimal influence of thermal activation at 523 K on the structural characteristics of MIL-100(Fe).[10] The fact that we can accurately reproduce rates upon cycling back and forth between various activation conditions used in these measurements further disproves the possibility of changes in turnover rates being associated with structural changes to the catalyst. The increasing turnover rates (per Fe^{2+} site) with thermal activation temperature observed here provide the first indication of active site non-uniformity in the MIL-100(Fe) sample under consideration. Materials activated at different temperatures, albeit exhibiting dissimilar rates, appear to be marked however by similar kinetic features, as reflected in rates remain first order in N_2O upon activation at both 423 and 523 K (Figure S3, SI). Moreover, turnover rates become decreasingly sensitive to reaction temperature with increasing extent of thermal activation (Figure 2b), pointing to alterations in enthalpies of reaction intermediates/transition states within the oxidation half cycle (steps 1 and 2, Scheme 1) upon thermal activation.

We reconcile the fact that Fe^{2+} sites in fully activated MIL-100 beds are uniform but those in partially activated ones are not by postulating that thermal treatments alter enthalpic landscapes within the oxidation half cycle on account of changes

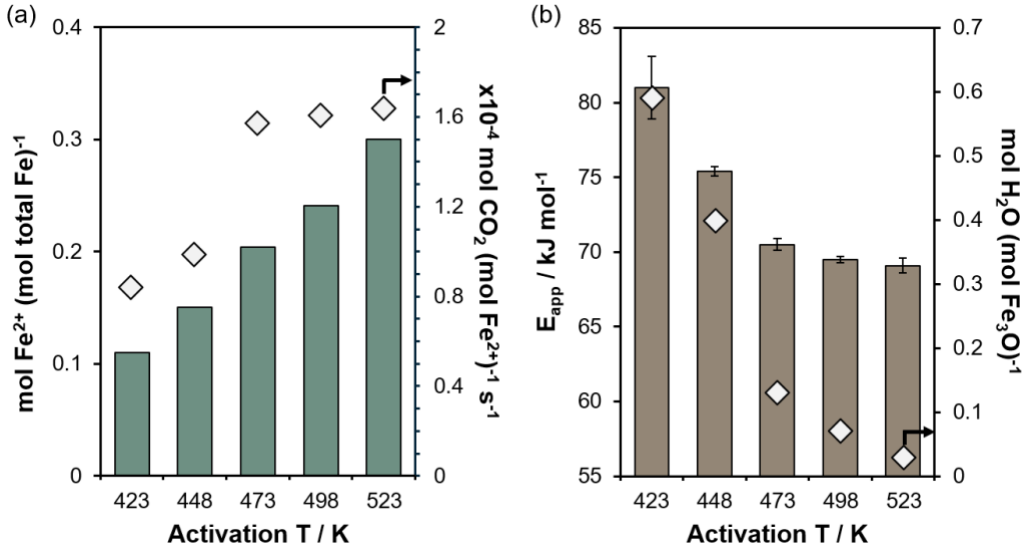

Figure 2. (a) Fe^{2+} open-metal site density and CO oxidation turnover rates as a function of activation temperature (reaction conditions: 423 K, 14.6 kPa N_2O, 1.5 kPa CO). Fe^{2+} site densities were measured using NO equilibrium breakthrough adsorption measurements completed previously.[10] (b) Apparent activation energy and the corresponding molar ratio of water to Fe_3O trimer node at each activation temperature (393 – 423 K, 14.6 kPa N_2O, 1.5 kPa CO). Samples were thermally activated under He flow (50 mL min^{-1}) for 12 hours at the temperature indicated.

in the degree of hydration of node. Charge balancing considerations dictate that as-synthesized samples contain one hydroxyl and two water ligands per trimer, and that fully activated beds contain Fe^{2+} sites on timer nodes that are completely dehydrated. Partially activated beds, on the other hand, are comprised not only of nodes that are either hydroxylated or dehydroxylated but instead contain a distribution of nodes that can be differentiated on the basis of their degree of hydration. Dehydroxylated nodes that contain Fe^{2+} sites that participate in oxidative turnovers can in principle be present in three distinct degrees of hydration (Figure 3): a fully dehydrated node containing no water or hydroxyl ligands in the coordination sphere of the trimer, a partially dehydrated node containing a water ligand and an open-metal Fe^{3+} site each, and a fully hydrated node carrying water ligands attached to both Fe^{3+} sites. Turnover rates that increase monotonically with thermal activation temperature can potentially be explained if beds with a greater average degree of hydration are less active compared to those with lower average degrees of hydration. Lumped rate constants at low N_2O/CO molar ratios ($\sim \leq 20$) where rates are first order in N_2O and zero order in CO represent the product of the equilibrium constant for N_2O adsorption and the intrinsic rate constant for oxo formation[34]:

$$\frac{r}{[Fe^{2+}]} = k_2 K_1 [N_2O] \qquad \text{(Eq. 1)}$$

where k_2 is the first order rate constant for N_2O decomposition ($Fe\cdots N_2O \rightarrow Fe\text{-}O + N_{2(g)}$) and K_1 the equilibrium constant for adsorption of N_2O onto an Fe^{2+} open-metal site. Enthalpic barriers that decrease with increasing activation temperature therefore suggest the relative stabilization of the oxo-formation transition state relative to the open-metal Fe^{2+} containing precursor state. The two methods used in our work to vary Fe^{2+} site densities are distinct in their propensity for altering the

degree of hydration of MIL-100 nodes: whereas titration experiments at varying NO pressures over fully activated samples only render available differing densities of Fe^{2+} sites all of which are present on fully dehydrated nodes, thermal treatments, on the other hand, generate Fe^{2+} active sites while concurrently creating a *distribution* of nodes the average degree of hydration of which increases with the severity of the thermal treatment that the material is subjected to. The average water loading of nodes vary significantly from approximately 0.6 to 0.03 mol H_2O (mol $Fe_3O)^{-1}$ when activated between 423 and 523 K (Figure 2b), providing a sufficiently large range of degrees of hydration that Fe^{2+}-driven oxidative turnovers can sense during CO oxidation experiments at 423 K. We next test

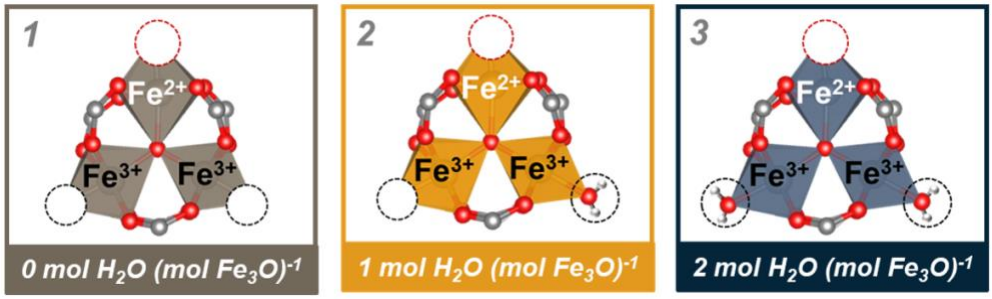

Figure 3. Three distinct dehydroxylated nodes each containing an Fe^{2+} site but unique in their respective degrees of hydration in that they contain zero (left), one (center), or two (right) water molecules coordinated to Fe^{3+} sites on the trimer node.

(using DFT) whether the presence of water in the coordination sphere of the iron trimer, but not necessarily in the immediate coordination sphere of the Fe^{2+} active site, can alter enthalpic barriers within the oxidation half cycle.

3.3. DFT evaluation of the effect of water ligation on oxidation half cycle kinetics. DFT calculations were conducted to evaluate enthalpy profiles for N_2O adsorption and oxo formation over MIL-100(Fe). MIL-100(Fe) structures chosen previously by Vitillo et al.[43] were used to evaluate the influence of water ligation onto triiron nodes on the enthalpies of four specific reaction intermediates and transition states – **A:** the isolated Fe_3O cluster, **AO:** N_2O adsorbed onto the Fe_3O cluster, **TS1:** the transition state for N-O bond scission, and **B:** the oxidized Fe_3O cluster containing the oxo moiety (Fe-O) and gaseous N_2. The enthalpy profile for these steps was evaluated for three separate water loadings (as illustrated in Figure 3) : Fe_3O – 0 H_2O, Fe_3O – 1 H_2O, and Fe_3O – 2 H_2O. Enthalpies of all intermediates and transition states (**AO**, **TS1**, and **B**) relative to the precursor state containing the activated node and gas phase N_2O (**A**) were found to increase with the degree of hydration of the node (Figure 4). Energies reported in Figure 4 are consistent with the postulate that the presence of water in the immediate coordination sphere of the node renders oxidation half cycles more kinetically demanding, and with lower turnover rates measured on samples subjected to less severe thermal activation protocols that result in beds carrying a higher average degree of hydration (Figure 2a). The increase in enthalpy values upon water ligation are greater for the oxo intermediate **B** (-26.7 kJ mol^{-1} for Fe_3O – 0 H_2O versus -20.1 kJ mol^{-1} for Fe_3O – 1 H_2O and -11.7 kJ mol^{-1} for Fe_3O – 2 H_2O) compared to chemisorbed N_2O **AO**, in which case there is only a slight increase in enthalpy values (-24.0 kJ mol^{-1} for Fe_3O – 0 H_2O versus -20.3 kJ mol^{-1} for Fe_3O – 1 H_2O and -19.5 kJ mol^{-1} for Fe_3O – 2 H_2O). Water ligation results in a more pronounced increase in enthalpy values for the oxo formation transition

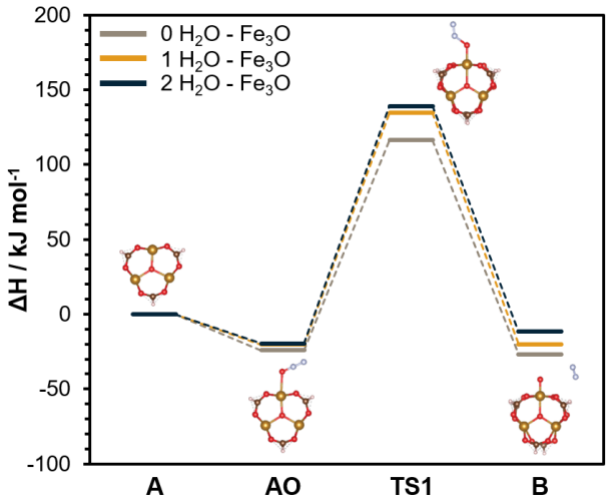

Figure 4. DFT-derived reaction energy diagram for N_2O decomposition over MIL-100(Fe) nodes. Enthalpies are reported at 1 atm and 298.15 K, and include the BSSE correction term. The reference state is intermediate **A**, which also includes a gaseous N_2O molecule (not shown). Only the intermediates for Fe_3O – 0 H_2O are shown in the plot; the N_2O decomposition and Fe-O formation intermediates for Fe_3O – 1 H_2O and Fe_3O – 2 H_2O are similar to Fe_3O – 0 H_2O, with the only difference being the H_2O content on each of the corresponding nodes.

state **TS1** (116.4 kJ mol^{-1} for Fe_3O – 0 H_2O versus 134.6 kJ mol^{-1} for Fe_3O – 1 H_2O and 139.2 kJ mol^{-1} for Fe_3O – 2 H_2O), and ligation of the first water molecule to form Fe_3O – 1 H_2O results in a larger increase in enthalpy compared to ligation of the second water molecule to form Fe_3O – 2 H_2O (Figure 4).

The influence of terminal ligands coordinated to trinuclear μ_3-oxo species (Figure 1) has been considered extensively for metal complexes with respect to electronic, magnetic, and adsorptive properties. Specifically, strong interactions between the individual metal ions and the central oxide ion of the M_3O unit provide a super exchange

pathway for magnetic coupling between the metal ions,[14,16] with Yaghi and coworkers demonstrating that such coupling interactions between metal ions is preserved within periodic MOF structures hosting $Fe_3O(CO_2)_2$ clusters.[50] Niedner-Schatteburg and coworkers previously reported a weakening of antiferromagnetic coupling between iron ions in trinuclear iron(III) acetate complexes due to increasing Fe-Fe distance and Fe-$O_{central}$ bond distance upon pyridine adsorption determined through a combination of Infra-Red-Multiple Photon Dissociation (IR-MPD) and Collision Induced Dissociation (CID) experiments.[19] These effects of geometric and magnetic coupling alterations resulted in pyridine binding energies that decreased significantly (from approximately 134 to 82 kJ mol^{-1}) with the addition of each ligand (n = 1, 2, or 3) to the iron core.

For MIL-100(Fe) evaluated here, both geometric (i.e. bond lengths) and electronic (i.e. charges) factors could potentially contribute to these differences in oxidation half cycle energetics (Section S2.3, SI). Subtle changes in the Fe-$O_{central}$ bond distance and Fe-Fe distance were observed for the intermediates upon water ligation (Tables S6-S8 and Figure S5, SI). Herein the discussion is focused on the Fe-$O_{central}$ bond distance between the Fe(II) site and the central, μ_3-O atom. Both **TS1** and **B** exhibit the most fluctuation in Fe-$O_{central}$ bond distance upon H_2O ligation, which coincides with the largest differences in the reaction energies (Figure 4). For **TS1**, Fe-$O_{central}$ bond distance also increased upon water ligation from 2.079 Å for Fe_3O – 0 H_2O to 2.164 Å for Fe_3O – 2 H_2O. For **B**, the Fe-$O_{central}$ bond distance also increased upon water ligation from 2.001 Å for Fe_3O – 0 H_2O to 2.024 Å for Fe_3O – 2 H_2O. These differences in Fe-$O_{central}$ bond distances (0.085 Å for **TS1** and 0.023 Å for **B**) agree with the similar values reported by Niedner-Schatteburg and coworkers for pyridine ligation.[19] Larger differences in Fe-Fe distances (~0.1 Å) are also observed upon water ligation (Figure S5). Minimal changes in the charges were observed for intermediates **A**, **AO**, **TS1**, and **B** upon water ligation (Table S6-S9, SI).

Additionally, we hypothesized that the presence of water in the coordination sphere of the trimer can alter antiferromagnetic coupling of electron spin between iron atoms present in the trimeric node. Specifically in the case of MIL-100(Fe) trimers, the Gagliardi and Bhan groups identified antiferromagnetic ($2S + 1 = 5$) configurations of iron centers as being energetically more stable and exhibiting lower DFT-calculated activation enthalpy barriers for N_2O decomposition compared to ferromagnetic ($2S + 1 = 15$) configurations.[51] We evaluated antiferromagnetic spin coupling for the iron-oxo intermediate B in hydrated, partially dehydrated, and fully dehydrated MIL-100(Fe) nodes using broken symmetry calculations in G16. Antiferromagnetic configuration electronic energies at each degree of hydration were found to be 24.9 to 31.1 kJ/mol lower than the corresponding ferromagnetic configuration electronic energy (Table S9, SI), in agreement with findings from prior work conducted by the Gagliardi and Bhan groups.[51]

Spin density difference plots indicate that addition of the first water molecule results in a decrease in alpha electron density and an increase in beta electron density on the central μ_3-O atom, with the addition of another water ligand further altering the alpha and beta electron densities (Figures S5 and S6, SI). These spin density plots therefore point to communication between water ligands and intermediates/transition states *through* the central μ_3-oxo bridge (as shown in Figure 5) despite the fact that the former are clearly removed from the immediate primary coordination sphere of the active site. This means of communication between ligands and reaction intermediates and transition states contrasts heavily with second sphere coordination effects reported in the prior literature wherein ligands external to the primary coordination sphere affect reaction free energy landscapes through *direct* physicochemical interactions with reactive species. Note that geometric constraints in the trimer node under consideration preclude water ligands bound to open-metal Fe^{3+} sites from interacting directly with the iron-oxo species; destabilization of the iron-oxo transition state relative to precursor **A** appears to instead occur by means of electronic communication through the Fe-O-Fe backbone reflected in spin density variations in the central μ_3-oxygen (Figure 5). DFT calculations discussed thus far are consistent with water ligation to MIL-100(Fe) nodes resulting in a suppression of oxidation rates through the relative destabilization of oxo-formation transition states. We next use in-situ spectroscopic and titration experiments to evidence the effect of second sphere ligand coordination on the structure of the M_3O node, and also on titrant adsorption characteristics and catalytic redox properties.

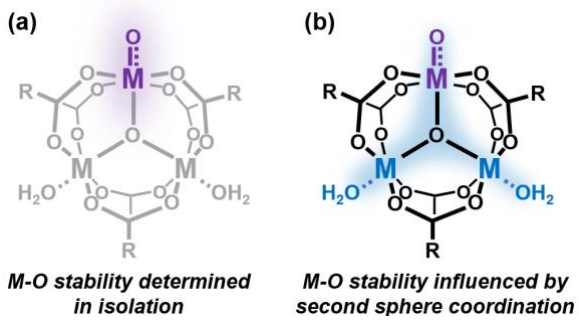

Figure 5. (a) Conventional and (b) proposed viewpoint for determination of the energy of the oxo-formation transition state. Whereas the conventional viewpoint considers the M-O bond in isolation from the rest of the trimer, the proposed viewpoint accounts for communication across the trimer μ3-O bridge that senses the presence of oxygenates on spectator M3+ ions.

3.4. XAFS analysis of structural changes to the MIL-100 node upon dehydration. As discussed in Section 3.3, prior literature as well as DFT calculations reported here indicate that geometric and electronic properties of μ_3-oxo centered metal trimers are influenced by the presence of coordinating ligands. Here, the local structure of the M_3O nodes of MIL-100(Fe) are evaluated experimentally using XAFS analysis to assess differences between the hydrated and fully thermally activated MIL-100(Fe) materials. In-situ analysis of MIL-100(Fe) samples under CO oxidation conditions was previously applied to assess the nature of

the iron-oxyl species formed.[34] In this work, we treated MIL-100(Fe) samples in-situ under inert flow at 523 K and then cooled them to 313 K for analysis to compare changes in node structure versus the as-synthesized material, with minimization of differences in temperature-dependent atomic vibrations present in measurements at a reaction temperature of 473 K.

The X-ray absorption near edge structure (XANES) of MIL-100(Fe) measured upon thermal treatment is consistent with a decrease in average iron oxidation state and expected formation of Fe^{2+} sites (Figure 6a), as observed previously,[34] with the heightened pre-edge feature in Figure 6b after thermal treatment also being consistent with loss of the centrosymmetric iron coordination geometry upon open-metal site formation.[52] Notably, cooling of the for MIL-100(Fe) sample from 523 K after thermal treatment to a lower temperature (313 K) for additional analysis results in only minor changes in the energy of the absorption edge and the pre-edge features (Figure 6a,b), suggesting that a majority of the Fe^{2+} and Fe^{3+} sites are retained in open-metal form during this step.

Extended x-ray absorption fine structure (EXAFS) fitting results considering the first shell M-O single scattering paths for MIL-100(Fe) are provided in Figures S7-S9 of the SI, and are summarized in Table 1. Analysis of the fitting results for both samples are consistent with the expected coordination geometry of the metal atoms (~ 5 coordinate), with the removal of labile water and hydroxide coordinated species upon thermal treatment resulting in the decrease in M-O coordination numbers in the activated samples (**Error! Reference source not found.Error! Reference source not found.**). It is noted that the discrepancies between S_0^2 (or S_0^2 x N) reported here (S_0^2 = 0.67 ± 0.10) and fit previously (0.79 ± 0.13)[34] for MIL-100(Fe) could be due to a thickness effect in the prepared samples, as discussed in Section S2.6 of the SI, although all spectra in each respective study are collected on the same sample, meaning that amplitude effects are constant and hence quantitative results can be accurately compared independently.

Additional qualitative analysis of changes in the local structure of the M_3O nodes in MIL-100(Fe) are evaluated in Figure 6, showing the real component of the Fourier transform, Re[χ(R)] for the samples before and after thermal treatment (Figure 6d). Specifically, the feature at low radial distance in Region (i) can be attributed to the first-shell Fe-O scattering path. Analysis of Region(i) indicates that upon thermal treatment, there is a small shift in the position of this peak to lower radial distances, consistent with an average decrease in first-shell Fe-O bond distances (Figure 6e). Similar trends were also observed from EXAFS fitting results described in Table 1, where estimated Fe-O distances are found to decrease upon thermal activation, although not outside the uncertainty of the fitted values. Moreover, the spectral feature in Region(ii) of Figure 6d has been attributed to Fe-Fe scattering paths based on the higher shell distance and the reverse Fourier transform spectra, Re[χ(q)] from R = 2.6 – 3.1 Å, indicating that this feature corresponds to heavier atoms that scatter more strongly at higher wavenumbers (Figure S10, SI). The spectra in this region for the thermally activated sample measured at both 523 and 313 K are spectroscopically distinct from the as-synthesized sample, suggesting that there may be changes in both Fe-Fe distances or the overall symmetry of the Fe_3O node

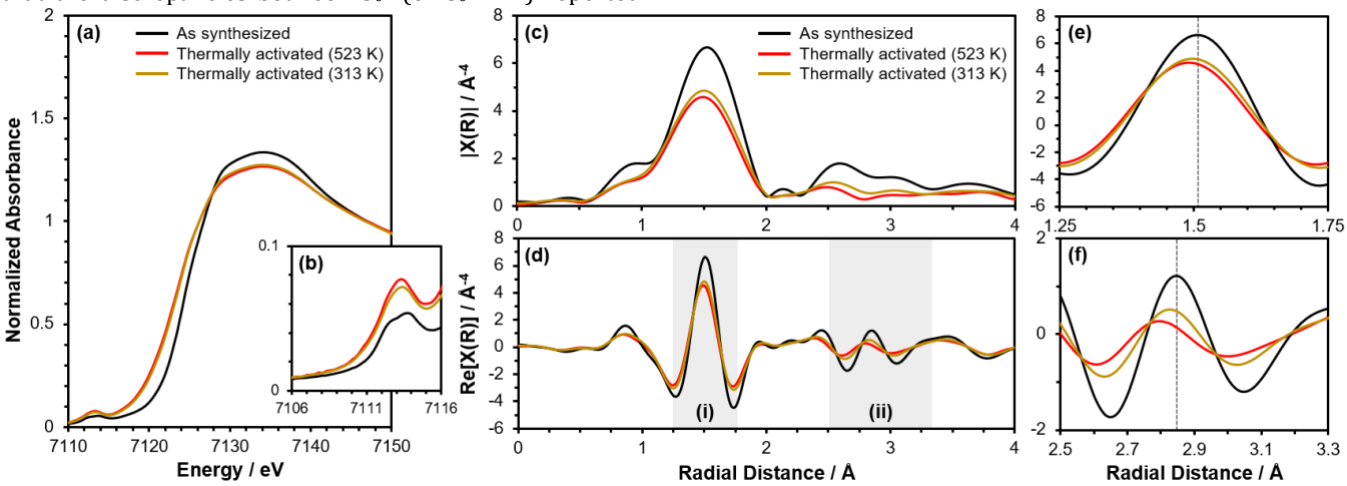

Figure 6. (a) Fe K-edge XAFS showing the XANES region for MIL-100(Fe) before and after thermal treatment at 523 K, where the thermally activated sample has been analyzed at temperature (523 K) and after cooling to near room temperature (313 K). (c) Magnitude and (d) real-component of the Fourier transform, k_3-weighted, spectra before and after thermal treatment (k = 3.1 – 10.6 $Å^{-1}$). Enlarged spectra of Regions (i) and (ii) of (d), respectively, in I and (f).

Table 1. Fe K edge EXAFS fit results (k = 3.1 – 10.6 $Å^{-1}$, Δk = 0.1, k^N N = 1,2,3, R = 1.1 – 2.1 Å), S_0^2 = 0.67 ± 0.10 fit for all samples simultaneously. For thermally activated samples, the temperature corresponds to the condition the spectra were measured. Notation: N – coordination number, R – distance to neighboring atom, σ^2 – mean square displacement, ΔE_0 - energy correction. R-factor by k-weight (k^1: 0.0018, k^2: 0.0026, k^3: 0.0048).

Sample	Path	N	R (Å)	σ^2 (x10^{-3} $Å^2$)	ΔE_0 (eV)

As Synthesized	Fe-O	6 (set)	1.985 ± 0.011	6.9 ± 1.6	-1.1 ± 1.9
Thermally Activated (313 K)	Fe-O	5.38 ± 1.10	1.974 ± 0.010	9.0 ± 1.7	-2.5 ± 1.5
Thermally Activated (523 K)	Fe-O	4.87 ± 1.07	1.967 ± 0.011	8.8 ± 2.0	

during this process (Figure 6f). Although the Fe-Fe or Fe-O distances in the thermally activated sample measured at 523 K may be influenced more so by thermal atomic vibrations, the spectra for the sample measured at 313 K following thermal treatment can be more directly compared to the as-synthesized sample measured at room temperature. Notably, the thermally activated sample cooled to 313 K still shows significant differences in both Region(i) and (ii) of the spectra in Figures 6d-f, suggesting that changes imparted to the geometry of the Fe_3O node were preserved upon cooling under inert flow. In MIL-100(Fe), the arrangement of iron atoms within the trinuclear core are characterized by an isosceles symmetry (Figure S11, SI).[37] Moreover, it is possible that additional losses in the overall symmetry of the node imparted by changes in coordination environment of the iron atoms (or the formation of one reduced iron center per node), may explain differences in the Fe-Fe scattering features observed for MIL-100(Fe) in **Error! Reference source not found.**.

Furthermore, the in-situ XAFS spectroscopy analyses are clearly suggestive of changes in the local structure of M_3O nodes upon thermal activation specifically as a consequence of changes in the coordination environment of metal sites within the trimer nodes. The characterization results presented here can be considered in the context of previous studies evaluating the influence of coordinated ligands (L) within trinuclear μ_3-oxo metallic complexes on geometric and electronic properties of the M_3O species (discussed in detail in Section 3.3), and aid in supporting the central postulate underlying this work aimed at identifying the impact of coordinated ligands on the adsorptive and catalytic redox properties of MIL-100 trimer nodes.

3.5. Influence of water ligation on NO binding. DFT calculations presented in Section 3.3 point to an effect of water ligation onto Fe^{3+} sites on the free energies of reaction intermediates and transition states in catalytic redox turnovers. We postulated that these second sphere coordination effects should in principle also extend to binding properties of titrants such as NO. NO serves as an Fe^{2+} site-selective titrant under a wide range of temperatures (423 – 488 K) – an aspect that enables accurate assessment of the contribution of divalent iron sites in alkane and CO oxidation.[10,51] Perturbations in NO binding can be sensed using infrared spectroscopic measurements as increases in the extent of backbonding into vacant NO π* orbitals that result in a weakening of the N-O bond are marked by a red-shift in the Fe^{2+}-nitrosyl vibration.[53–56] This marked sensitivity of the nitrosyl stretching frequency to the strength of NO binding helps us use changes in the latter to sense second sphere coordination effects in lieu of exacting heats of adsorption measurements that would require either calorimetric data or adsorption isotherm measurements over a wide range of temperatures and NO pressures.

Exposure of MIL-100(Fe) to 0.5 kPa NO at 423 K results in the appearance of an Fe^{2+}-mononitrosyl band centered near 1808 cm^{-1} (Figure 7a), in line with in-situ infrared spectroscopy measurements on MIL-100(Fe) reported by other groups,[51,57,58] and with our own analysis in which the entirety of the Fe^{2+} site pool created regardless of the tested thermal

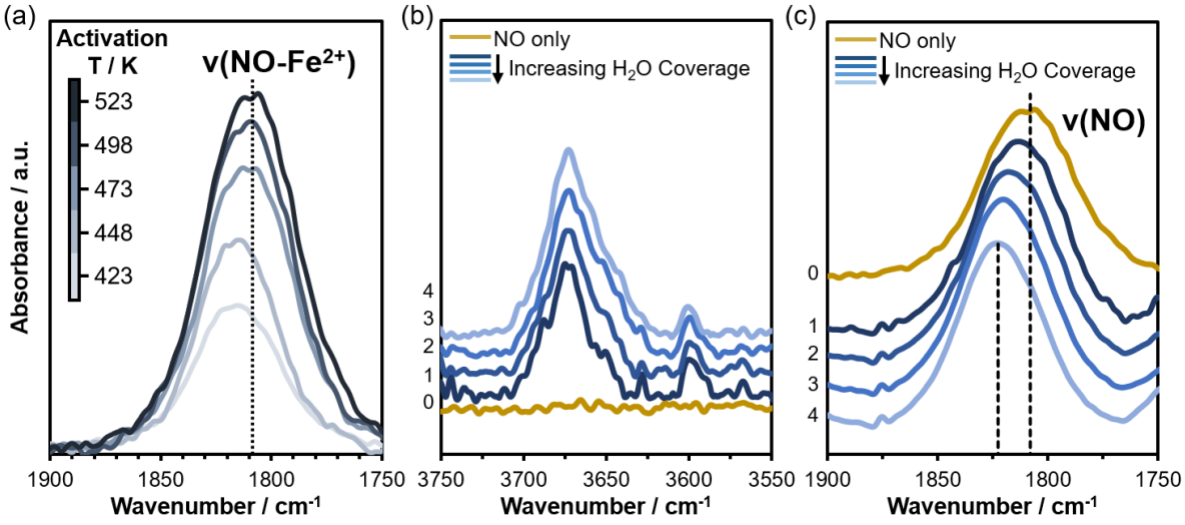

Figure 7. (a) Infrared spectra of NO adsorption (0.5 kPa) at 423 K over MIL-100(Fe) thermally activated under He flow. (b) ν(NO) and (c) ν(OH) portions of the IR spectrum under NO flow (0.5 kPa) and upon introduction of 2 μL injections of H_2O (~ 1 mol H_2O (mol Fe)$^{-1}$) at 423 K.

activation temperature used were found to be saturated with nitrosyls at the temperature and NO pressure under consideration.[10] The intensity of the Fe^{2+}-nitrosyl band is not, however, the only spectroscopic parameter that varies

with activation temperature; infrared data in fact indicate a monotonic redshift with increasing activation temperature (Figure 7a), indicative not only of an increase in nitrosyl density but also a perturbation in the extent of backbonding interactions on samples that are more thoroughly dehydrated.

Further evidence of the effect of second sphere water on NO binding was obtained by dosing water into an IR cell containing a fully activated sample treated at 523 K with NO in the gas phase helping create an Fe^{2+}-nitrosyl saturated surface. The injection of 2 μL aliquots of water into the IR cell at 423 K under a 0.5 kPa NO flow resulted in a systematic increase in degree of hydration reflected in a monotonic increase in area of the band at 3672 cm^{-1} assigned previously to asymmetric stretching vibrations of coordinated water molecules (H_2O-Fe^{3+}) in MIL-100(Fe) (Figure 7b).[7,10,57,59] This increase in degree of hydration appears to occur in the absence of determinative changes in NO coverage inferred from very minor increases in intensity of the O-H band at 3581 cm^{-1} assigned to hydroxides (Fe^{3+}-OH^-) that would have been formed through H_2O dissociation over Fe^{2+} sites.[10] These negligible changes in Fe^{2+} site density are further reinforced by the recalcitrance of the nitrosyl band to MIL-100(Fe) hydration which should have exhibited more perceptible decreases if displaced by hydroxyl species (Figure 7c and Figure S13b, SI). Progressive hydration of the sample, however, results in a monotonic blueshift of the nitrosyl band from 1808 cm^{-1} for the fully dehydrated sample to 1823 cm^{-1} for the most heavily hydrated one in which Fe^{3+} sites are almost completely saturated with water. Note that whereas the blueshift noted in Figure 7c upon hydration or the redshift observed upon thermal activation in Figure 7a can each potentially arise from coordination and elimination, respectively, of water molecules involved in proximal binding interactions with nitrosyl species, the combination of these two observations render such direct effects unlikely due to the fact that water molecules that are more strongly bound would be desorbed at higher temperatures but also adsorbed preferentially during the hydration experiments. We assert instead that the correlation between growth of the asymmetric stretching band corresponding to Fe^{3+}-bound water and the blueshift in nitrosyl frequency, combined with complementary trends observed upon thermally activating the sample under inert flow provide corroborating evidence for second sphere coordination effects on NO binding.

In fact, not only does the presence of water in the secondary coordination sphere perturb NO binding but it does so to an extent that alters the reversibility of the binding process itself. NO adsorbs irreversibly at 423 K onto a sample fully thermally activated at 523 K, as demonstrated previously using in-situ titration experiments with MIL-100(Fe) during CO oxidation with N_2O.[34] Rate recoveries upon elimination of titrant were tested as a function of the degree of hydration of nodes controlled by means of varying thermal treatment temperature; whereas irreversible binding of the titrant should result in negligible rate recoveries, reversible titrant binding should result in significant rate recoveries on the timescale of catalytic turnovers. Rate recoveries remain minor (at less than 4%) for the sample treated at 523 K, and also for samples activated at 473 and 498 K which show recoveries of less than 6 and 5%, respectively (Figure 8). Much larger fractions – 18 and 23% of the steady state turnover rate – can be recovered over catalysts treated at 448 and 423 K, respectively, suggesting that the presence of hydrated nodes imparts reversibility to NO adsorption onto MIL-100(Fe) at 423 K. These quantities of NO adsorbed irreversibly versus reversibly at each activation temperature were quantified using the total quantity of NO adsorbed estimated from NO breakthrough measurements[10] and using NO temperature-programmed desorption (TPD) measurements following purging of reversibly bound NO at 423 K in which NO desorbs in a 423 – 488 K range (Figure S5, SI) – similar to the temperature range for the desorption of Fe^{2+}-nitrosyls hosted on ZSM-5 (400 – 650 K).[60] Partitioning the Fe^{2+} active site pool into these two types of sites indicates that at 423 K increasing fractions of Fe^{2+} sites adsorb NO irreversibly with increasing treatment temperature (Figure Sxy, SI), in line with rate recovery trends in Figure 8.

3.6. Deconvoluted turnover rates for Fe^{2+} sites in dehydrated, partially hydrated, and fully hydrated nodes. NO binding

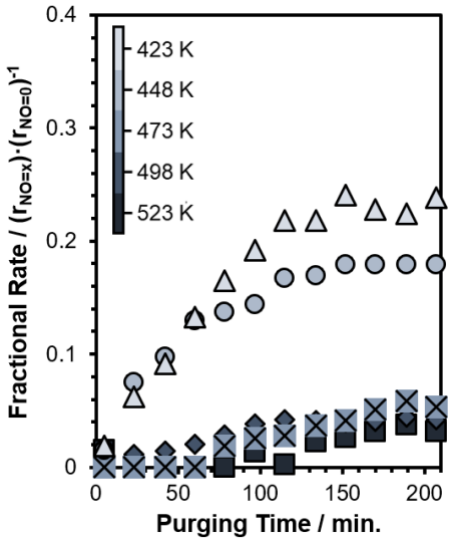

Figure 8. Fractional rate recoveries following titration with 0.5 kPa NO under reaction conditions (423 K, 14.6 kPa N_2O, 1.5 kPa CO); 0.5 kPa NO is replaced with inert at time zero and the oxidation rate measured ($r_{NO=x}$) normalized by the steady state rate in the absence of titrant ($r_{NO=0}$).

events that become increasingly irreversible at 423 K with the severity of thermal treatment indicate that NO binding onto fully hydrated and fully dehydrated nodes at this temperature are reversible and irreversible, respectively. The contribution of partially hydrated nodes carrying only one water molecule per node may appear to be ambiguous, but becomes clearer upon closer inspection of the rate data. Turnover rates for active site pools that differ from the standpoint of the reversibility of NO binding can be obtained from the ratio of rate contributions obtained from fractional rate recovery data (Figure 8) and site distributions derived from TPD measurements (Figure S15, SI). Turnover rates for sites that bind NO irreversibly

at 423 K are threefold higher than those for sites that bind NO reversibly (Figure 9). Moreover, both sets of sites exhibit turnover rates that vary only minimally with thermal activation temperature, suggesting that either only two sets of sites contribute to the rate at the average water loadings explored, or that two of the three sites under consideration – all of which are abundant in our experiments – turn over at rates that are highly similar.

Given that irreversible NO binding sites constitute the largest fraction of Fe^{2+} sites in the nearly fully dehydrated catalyst sample activated at 523 K, we assume that the entire density of Fe^{2+} open-metal sites within nodes containing 0 coordinated water molecules – termed Site 1 (Fe_3O – 0 H_2O) – bind NO irreversibly at 423 K. Given the statistical probability of low H_2O to Fe_3O node ratios producing predominantly nodes with 0 to 1 ligated water molecules, it is assumed that Fe^{2+} open-metals sites within nodes with 1 coordinated water molecule, Site 2 (Fe_3O – 1 H_2O), bind NO reversibly at 423 K. This assumption is supported by the parity between the average water loading in the MOF bed and the fraction of Fe^{2+} sites that bind NO reversibly (Figure S16, SI). Moreover, it has been observed from infrared spectroscopic characterization of NO adsorbed onto MIL-100 Fe^{2+} open-metal sites that the frequency of the ν(NO) band corresponding to Fe^{2+}-nitrosyls increases systematically with increasing water coverage, evidence of weaker average binding of NO. It can therefore be expected

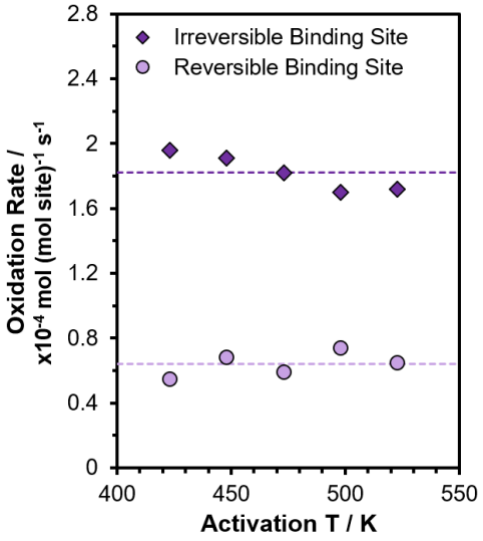

Figure 9. The oxidation rate attributed to Fe^{2+} sites that bind NO reversibly versus irreversibly at 423 K for samples activated at various temperatures, determined from the experiments in Figure 8 and Figure S14. (Reaction conditions: 423 K, 14.6 kPa N_2O, 1.5 kPa CO). Dashed lines represent the average oxidation rate for the irreversible and reversible binding sites across the five activation conditions evaluated.

that Fe^{2+} open-metal sites within iron nodes with 2 coordinated water molecules, or Site 3 (Fe_3O – 2 H_2O), may bind NO even more weakly than Site 2.

Bare nodes that are completely dehydrated are much more abundant than partially hydrated ones at low water loading values, meaning that the formation of partially hydrated nodes through adsorption of water onto fully dehydrated nodes is much more likely from a mere statistical standpoint compared to adsorption of water onto a partially hydrated node to form a fully hydrated one. A minority of sites being present in a fully hydrated state are further reinforced by comparisons of site fractions with binomial distributions presented in Figure 10. Of the three types of sites present, fully hydrated ones are both the least predominant at the water loadings tested, and also the least active, resulting in turnover rates for (ir)reversible binding sites that remain near-invariant in activation temperature (Figure 9). These turnover rates reflect for the most part simply the catalytic propensities of sites on nodes that carry either one molecule of water ($TOF_{reversible}$) or those that are fully dehydrated ($TOF_{irreversible}$). The low water loadings accessed using thermal treatment protocols used here therefore, somewhat fortuitously, evidence partially hydrated nodes to be characterized by reversible, not irreversible NO binding, because relatively inactive fully hydrated sites are too scarce to account for the significant fractional rate recoveries observed in Figure 8. The scarcity (and relative inactivity) of fully hydrated sites are further reinforced by deconvoluted site distributions and turnover rates presented below that are obtained independently from regression against rate data over a broader range of water loadings.

The experimentally measured oxidation rate per Fe^{2+} site can be expressed as the sum of contributions from the three distinct sites:

$$\frac{r_{CO_2}}{Fe^{2+}} = x_1\left(\frac{r_{CO_2}}{Fe^{2+}}\right)_{Site\ 1} + x_2\left(\frac{r_{CO_2}}{Fe^{2+}}\right)_{Site\ 2} + x_3\left(\frac{r_{CO_2}}{Fe^{2+}}\right)_{Site\ 3} \quad \text{(Eq. 2)}$$

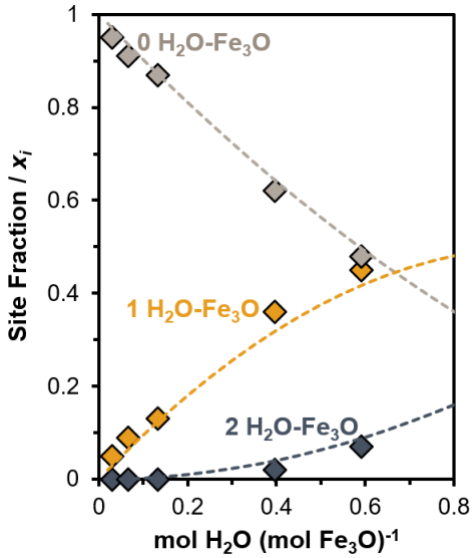

Figure 10. Estimated fractions of Site 1 (0 H_2O-Fe_3O), Site 2 (1 H_2O-Fe_3O), and Site 3 (2 H_2O-Fe_3O) for MIL-100(Fe) as a function of the H_2O to Fe_3O molar ratio. Dashed lines represent site fractions estimated for a binomial distribution.

where x_1, x_2, and x_3 represent the fractional densities of Fe^{2+} sites containing 0, 1, and 2 water molecules in the second coordination sphere, respectively, and the terms in parentheses represent individual turnover rates for each of these sites. Moreover, the total water loading in the bed

equates to the sum of the water molecules present in partially and fully hydrated nodes as follows:

$$\frac{(mol\ H_2O)}{(mol\ Fe_3O)} = x_2 + 2x_3 \qquad \text{(Eq. 3)}$$

Equation 3, combined with the fact that x_1 is merely the fraction of NO adsorbed irreversibly, and that site fractions sum up to a value of unity, provide three equations that allow for the explicit calculation of site fractions accessed as a function of activation temperature. Site distributions thus calculated track closely with the predicted binomial distribution of the three sites (Figure 10), suggesting little thermodynamic preference for the binding of water as a function of the degree of hydration of the node. This consistency with the calculated binomial distribution aligns with DFT calculations reported by Vitillo and Gagliardi in which enthalpies for water adsorption onto MIL-100(Fe) triiron nodes decreased only marginally as a function of degree of hydration, bearing values of -74, -72, and -65 kJ mol^{-1}, respectively, for nodes with 0, 1, or 2 water molecules.[44] Such minor differences in binding energies are consistent with the lack of preference shown for water adsorption onto nodes that are either partially or fully dehydrated.

Kinetic measurements at elevated water to node molar ratios inaccessible through thermal activation were completed by co-feeding specific partial pressures of water vapor during reaction of CO with N_2O. Water breakthrough measurements were used to quantify the total amount of water adsorbed onto the fully activated catalyst (treated at 523 K) at a given water vapor partial pressure (Figure S6a, SI), and residual Fe^{2+} site densities determined using NO titrations (Figure S6c, SI) allowed for the deconvolution of water molecules adsorbed dissociatively onto Fe^{2+} sites as hydroxyls versus those adsorbed molecularly onto Fe^{3+}. Table 2 lists the total quantity of water and NO adsorbed, as well as the water loadings achieved at the water partial pressures tested, with water loadings obtained using this procedure spanning a relatively wide range of values between 1.02 and 1.95 mol H_2O (mol Fe_3O)$^{-1}$.

Unlike experiments on thermally treated samples, eliminating NO from the gas phase in the presence of water vapor leads to the displacement of nitrosyls, preventing analysis of fractional rate recoveries. Furthermore, we assume that site distributions follow the binomial distribution at high mol H_2O (mol Fe_3O)$^{-1}$ ratios ($0.59 < x \leq 2$) given the consistency with the same at water loadings below 0.59 mol H_2O (mol Fe_3O)$^{-1}$. The fractional density of sites with 0, 1, or 2 molecules of water can be estimated using equation 3 combined with the fact that site fractions add up to unity, and the binomial distribution predicted value of site 3 represented by the following equation:

$$x_3 = 0.25\left(\frac{mol\ H_2O}{mol\ Fe_3O}\right)^2 \qquad \text{(Eq. 4)}$$

Turnover rates over Fe^{2+} sites on nodes carrying 0, 1, or 2 water molecules were determined by regressing against the rate data in Figure 11 and assuming that site distributions follow the binomial distribution across all water to node ratios. Turnover rates were obtained by minimizing the weighted (weight = inverse of the measured overall oxidation rate) sum of squared residuals (SSR) between the measured and estimated overall formation rates. Estimated turnover rates over partially and fully hydrated nodes are 77 and 97% lower than those over dehydrated nodes (Table 3). This drastic decrease in turnover rates upon hydration explain the heterogeneity evident in the Fe^{2+} active site pool inferred from the measured turnover rates reported in Figure 2, and are consistent with increases in DFT-derived activation enthalpy barriers upon hydration captured in Figure 4. The analysis presented here provides quantitative estimates of deconvoluted turnover rates for each of the individual sites carrying the same primary coordination environment but differing in secondary sphere water content.

3.7. Amplifying second sphere effects through titrations and changes in oxygenate identity. The presence of water in the hydration sphere of the MIL-100(Fe) node destabilizes not only oxo formation transition states within the oxidation half cycle but also NO adsorption (Sections 3.3 and 3.5); in fact, NO binding is perturbed to an extent that renders its binding at 423 K to be irreversible, evidenced in part through a blueshift in the Fe^{2+}-nitrosyl infrared band with progressive activation at higher temperatures (Figure 7). This weakening of NO binding sensed in the NO TPD and fractional rate recovery experiments reported in the previous section imply that preferential NO binding onto Fe^{2+} sites on fully dehydrated nodes at low NO pressures precedes adsorption onto partially and fully hydrated nodes that occurs at higher NO pressures. Maintaining an appropriate pressure of NO that selectively saturates the fraction of nodes in the bed that are dehydrated while retaining a meaningful population of unoccupied Fe^{2+} sites on nodes that are either partially or fully hydrated can help amplify second sphere effects by selectively eliminating turnovers on nodes devoid of second sphere oxygen in the form of bound water.

Measured turnover rates at 488 K on a sample fully thermally activated at 523 K decrease linearly with nitrosyl coverage when the latter are controlled by varying NO pressures between 0.003 and 0.02 kPa (Figure 12) because titrated sites are characterized by the same turnover rate as residual sites that

Table 2. Total water adsorbed, NO adsorbed, and water loadings obtained under various water co-feed pressures during the oxidation of CO with N_2O; reaction conditions: 423 K, 14.6 kPa N_2O, 1.5 kPa CO.

Water Partial Pressure / kPa	Total H_2O Adsorbed / mol (mol Fe)$^{-1}$	NO Adsorbed / mol (mol Fe)$^{-1}$	H_2O Adsorbed to Fe^{3+} OMS/ mol (mol Fe)$^{-1}$	mol H_2O (mol Fe_3O)$^{-1}$
0.15	0.42	0.21	0.33	1.02
0.35	0.60	0.10	0.40	1.26
0.54	0.75	0.06	0.51	1.56
0.78	0.92	0.02	0.64	1.95

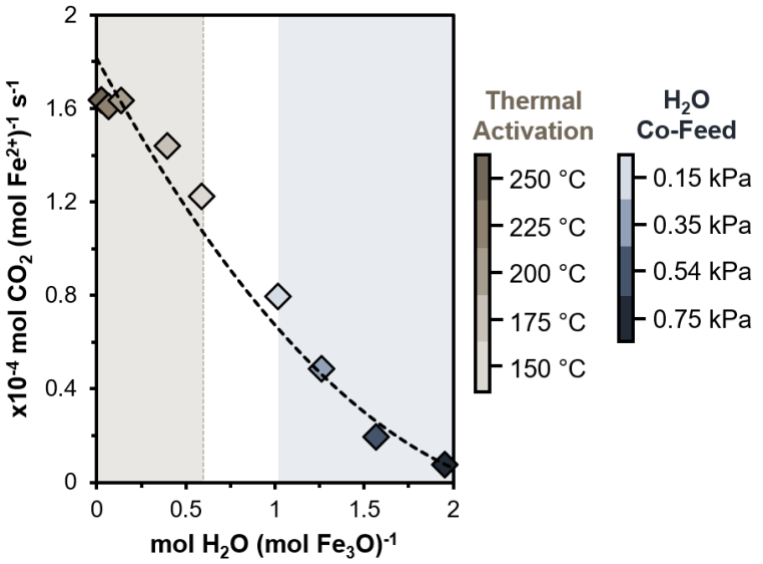

Figure 11. Turnover rates as a function of the water to Fe_3O molar ratio varied through thermal treatment or using H_2O co-feeds (14.6 kPa N_2O, 1.5 kPa CO, 423 K). The dashed line represents rates estimated from regressed turnover rates for Site 1, 2, and 3 (Table 3).

Table 3. Turnover rate estimated for Fe^{2+} open-metal sites within Fe_3O nodes with 0, 1, or 2 water molecules, estimated from the data in Figure 10.

Site Identity	Turnover Rate / $x10^{-4}$ mol (mol Fe^{2+})$^{-1}$ s^{-1}
Site 1 (Fe_3O-0H_2O)	1.816 ± 0.190
Site 2 (Fe_3O-1H_2O)	0.409 ± 0.043
Site 3 (Fe_3O-2H_2O)	0.060 ± 0.006

remain untitrated at any given NO pressure. This uniformity is merely a reflection of the fact that all Fe^{2+} sites in a fully thermally activated bed are equivalent in their propensity toward NO binding and CO oxidation. Rates under identical conditions – except with a 0.35 kPa water co-feed (H_2O:Fe_3O = 1.08, Table 4) and an active site density of 0.23 mol Fe^{2+} (mol Fe)$^{-1}$ – result in a strong non-linear decrease in rates as a function of nitrosyl coverage, with initial changes in coverage having a disproportionate impact on measured turnover rates (Figure 12). Dehydrated nodes that bind NO more strongly at lower coverages also turn over at faster rates (Figure 11 and Table 3), meaning that residual sites available at any given NO coverage or pressure are more heavily hydrated compared to titrated sites, and therefore turn over (on average) at slower rates. These titration data are consistent with second sphere effects of water on NO binding and CO oxidation inferred quantitatively in Section 3.5, and suggest that maintaining in the gas phase an appropriate pressure of a titrant such as NO that binds preferentially to dehydrated sites provides a strategy for arresting beds in states where second sphere effects predominate, even on beds activated under conditions that create a broad distribution of nodes differing in second sphere oxygen content.

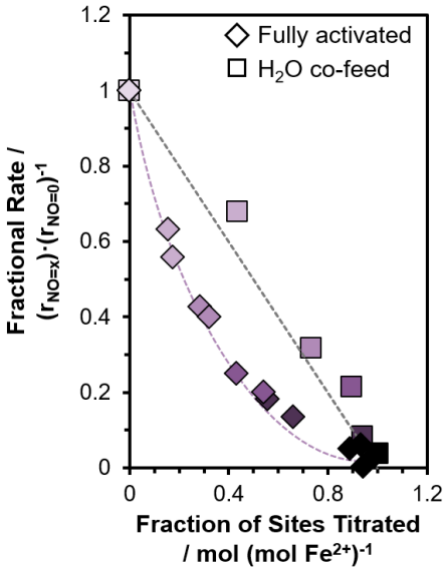

Figure 12. Fractional rates as a function of the fraction of Fe^{2+} open-metal sites titrated (0.003 – 0.2 kPa NO, reaction conditions: 14.5 kPa N_2O, 1.5 kPa CO, 488 K) over MIL-100(Fe) activated at 523 K, with and without H_2O co-feed (0.35 kPa). Data for the fully activated sample (without H_2O co-feed) are reproduced from ref. [34].

Table 4. Under water co-feed, the quantity of water adsorbed, the remaining density of Fe^{2+} open-metal sites (determined by NO titration), and the corresponding H_2O to Fe_3O node molar ratios (0.35 kPa H_2O co-fed during reaction at 215 °C, 2.9 kPa N_2O, 1.5 kPa CO).

mol H_2O adsorbed (total mol Fe)$^{-1}$	Fe^{2+} Site Density / mol (total mol Fe)$^{-1}$	mol H_2O (mol Fe_3O)$^{-1}$
0.42	0.23	1.08

As noted in sections 3.3, 3.5, and 3.6, second sphere effects mediated by bound water in the absence of direct physiochemical interactions with intermediates and transition states destabilize oxo-formation transition states within the oxidation half cycle relative to the Fe^{2+} precursor state. The kinetics of oxo-formation over MIL-100(Fe) therefore appear to be driven not merely by the oxophilicity of the Fe^{2+} site in isolation, but instead by a shared oxophilicity that is distributed across the trimeric node, presumably through the μ_3-ox' 'juncti'n' linking the three metal atoms (Figure 5). We posit that the oxophilicity of relevance to the reactivity of the MIL-100(Fe) node is not merely thIhich characterizes the propensity of the Fe^{2+} site (in isolation) to interact with oxygen, but instead a shared, distributed oxophilicity that can also alternatively be satiated in part through binding of an oxygenate such as water to Fe^{3+} sites that would otherwise be expected to be spectating in function. Oxygenates that satiate this oxophilicity more effectively can therefore be expected to result in a larger diminution in oxidation rates.

Fe-oxo formation occurs through electron transfer from open-metal iron in a reduced state to added oxygen that is electrophilic in nature with respect to the triiron node. Binding of molecular water ligands, on the other hand, is driven by electron transfer from oxygen to Lewis acidic open-metal Fe^{3+} sites. This electron donation into the triiron node destabilizes the oxo-formation transition state (formed through electron transfer *away* from the Fe^{2+} site) relative to the precursor state devoid of added oxygen. Turnover rates over the partially hydrated node are lower than those over the dehydrated node due to this destabilization, and decrease further upon addition of the second water molecule because coordination of a single water molecule only partially satiates the oxygen carrying capacity of the node. This incomplete satiation of the oxophilicity of the trimer suggests that choosing oxygenates with a greater propensity for electron transfer into the node should amplify rate diminution through second sphere interactions. Measured turnover rates at identical bed oxygenate loadings (0.48 – 0.52 mol R-OH per mol Fe_3O, Table S2, SI) for four different alkanols varying in alkyl chain length – water, methanol, ethanol, and isopropanol – decrease monotonically with alkanol proton affinity (Figure 13), suggesting that longer chain alcohols destabilize oxo-formation transition states more effectively than shorter chain ones. Isopropanol – the alkanol carrying the highest proton affinity, i.e. the highest enthalpy gain upon coordination to a gas phase proton – also results in the largest enthalpic destabilization of the oxo-formation transition state as reflected in apparent activation energy values that are 9 and 17 kJ mol^{-1} higher than for hydrated and fully dehydrated beds, respectively (Table 5). These effects of oxygenate identity on oxidation rates help relate the magnitude of second sphere effects with the basicity of the ligand, and help emphasize the generality of these effects which seem to extend to oxygenates other than water. As discussed next, these second sphere effects are general enough that they appear to extend beyond oxidation half cycles involving M-O bond formation, and continue to affect catalytic turnovers even after the active site enters into the reduction half cycle comprised of M-O bond scission steps.

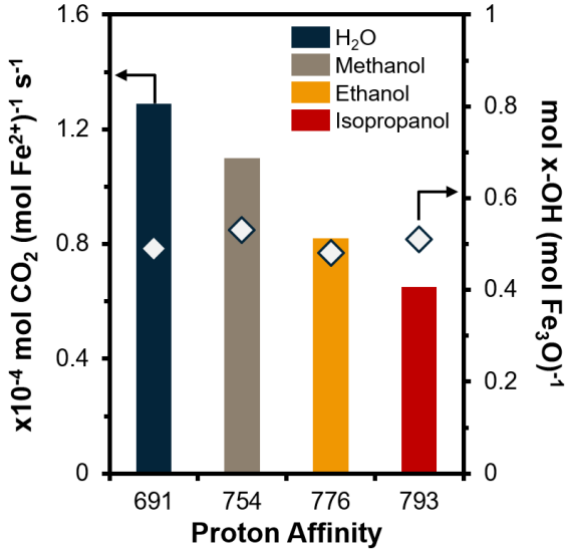

Figure 13. Effect of oxygenate identity, with increasing proton affinity (NIST Database: Hunter & Lias, *J. Phys. Chem. Ref. Data* (1998)), on the CO oxidation turnover rate at similar molar ratios of oxygenate (x-OH) to Fe_3O nodes. (14.6 kPa N_2O, 1.5 kPa CO, 423 K).

Table 5. Apparent activation energy for fully dehydrated MIL-100(Fe) (treated at 523 K for 12 h under He flow, prior to reaction) and under conditions of partial ligation with water or isopropanol (reaction conditions: 14.6 kPa N_2O, 1.5 kPa CO, 393 – 473 K).

Ligand (x-OH)	mol x-OH (mol Fe_3O)$^{-1}$	E_{app} / kJ mol^{-1}
No ligand	N/A	69.1 ± 0.5
Water	0.49	77.8 ± 1.0
Isopropanol	0.51	86.2 ± 1.7

3.8. Second sphere effects within oxidation and reduction half cycles over MIL-100(Cr). Steady state and transient kinetic, isotopic, and in-situ titration data are consistent with CO oxidation over MIL-100(Cr) proceeding over divalent Cr sites through an identical sequence of elementary steps as on MIL-100(Fe), but with much larger oxo coverages resulting from an attenuated imbalance between kinetic demand for the oxidation versus the reduction half cycle.[34] Oxygen coverages remain less than about 43% under a N_2O:CO molar ratio of 50 at 473 K on MIL-100(Fe) due to the demanding nature of oxidation half cycle steps that render reduction half cycle steps in both CO and methane oxidation to be kinetically irrelevant. Significant oxygen coverages are sensed over MIL-100(Cr) under identical conditions due to reduction half cycle steps that are more kinetically demanding relative to oxidation half cycle steps than over MIL-100(Fe). For example, M-O coverages for M^{2+} sites at an N_2O/CO ratio of 1 at 473 K are estimated to be roughly 1.4% and 92% for the iron and chromium isostructures, respectively, based on previously

estimated kinetic parameters.[34] Equation 5 captures steady state kinetic features between 393 and 473 K for MIL-100(Cr), with the fractional coverage of oxo species at any reaction condition of interest determining the sensitivity of rates to N_2O and CO pressure:

$$r = \frac{\frac{k_2K_1[N_2O]}{1+\frac{k_2K_1[N_2O]}{\overrightarrow{k_3}[CO]\left(1-\frac{\overleftarrow{k_3}}{\overleftarrow{k_3}+k_4}\right)}}}{1+\frac{k_{ox}[N_2O]}{k_{red}[CO]}} = \frac{k_{ox}[N_2O]}{1+\frac{k_{ox}[N_2O]}{k_{red}[CO]}} \qquad \text{(Eq. 5)}$$

where the ratio of the apparent rate constants for the oxidation and reduction half cycles can be expressed as the following functions of the intrinsic rate constants:

$$k_{ox} = k_2K_1 \qquad \text{(Eq. 6)}$$

and

$$k_{red} = \overrightarrow{k_3}\left(1-\frac{\overleftarrow{k_3}}{\overleftarrow{k_3}+k_4}\right) \qquad \text{(Eq. 7)}$$

in which steps 1, 2, 3, and 4 represent N_2O adsorption, oxo formation, CO adsorption, and C-O bond formation elementary steps, respectively. Note that k_{ox} is comprised solely of rate constants within the oxidation half cycle, and k_{red} is determined exclusively by rate constants within the reduction half cycle, and that it is the ratio of these apparent rate constants at a given N_2O:CO ratio that determines oxo coverages and reaction orders. This partition between rate parameters in the two half cycles enables analysis of second sphere effects without the need for a deconvolution of rate constants for steps in which metal-oxygen bonds are formed versus cleaved.

Cr^{2+} sites on samples activated at 523 K resulting in 0.14 mol H_2O (mol Cr_3O)$^{-1}$ appear to be uniform in nature, as evidenced by normalized oxidation rates that decrease non-linearly with time but linearly with fractional methoxy coverages during titration with methane (Figure S17, SI). Titrations with methane are used here in-lieu of NO titrations given the lack of NO binding onto divalent Cr sites in MIL-100(Cr) between 423 and 473 K,[11] and the stoichiometric nature of reduction half cycles mediated by methane,[10,11] in contrast with catalytic cycles effected by CO. Methoxy intermediates formed during CH_4-induced reduction half cycles can be quantified on the basis of the moles of ethanol formed upon introduction of methanol into the catalyst bed after purging under inert at 373 K.

Analogous to MIL-100(Fe) beds, MIL-100(Cr) beds subjected to increasingly severe thermal treatments result in turnover rates per Cr^{2+} site that increase monotonically with activation temperature (Figure S18, SI). Unlike MIL-100(Fe), however, sensitivities of oxidation rates to N_2O and CO were also found to be affected by thermal activation; whereas rates over the Fe variant remain first order in N_2O regardless of the treatment temperature used and degree of hydration achieved (Figure S3, SI), rates over the Cr analogue exhibit an increasing dependence on CO pressure and a concurrent decreasing dependence on N_2O pressure that is indicative of higher oxo coverages achieved on less heavily dehydrated beds accessed at higher thermal treatment temperatures (Figure 14). In fact, the more balanced kinetic limitations encountered on MIL-100(Cr) but not on MIL-100(Fe) are only encountered on beds that are more thoroughly dehydrated, with beds carrying significant amounts of water mimicking in kinetic behavior MIL-100(Fe) beds in which oxidation half cycle steps are disproportionately demanding.

Steady state kinetic data over MIL-100(Cr) can be accurately described using equation 5 irrespective of thermal treatment or water loading (Figure S19, SI), except with differing lumped oxidation and reduction kinetic parameters k_{ox}

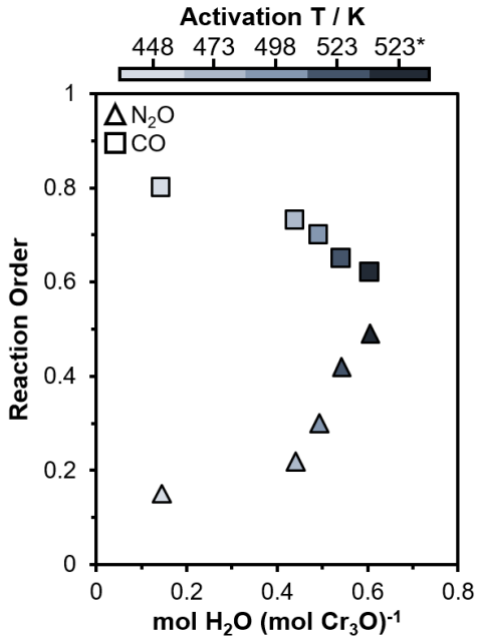

Figure 14. N_2O reaction orders (at 31 kPa CO) and CO reaction orders (at 8.7 kPa N_2) at a reaction temperature of 448 K over MIL-100(Cr) samples activated at the indicated temperature under He flow or in vacuum (indicated by *).

and k_{red}. The oxidation half cycle rate constant k_{ox} decreases by more than a factor of 5 upon increasing the water loading from 0.14 to 0.61 mol H_2O (mol Cr_3O)$^{-1}$, and the reduction half cycle parameter exhibits an almost twofold decrease for an equivalent increase in water loading (Table 6). Unlike triiron nodes in MIL-100(Fe) in which only oxidation half cycle parameters are kinetically relevant, binding of water into the coordination sphere of the chromium trimer destabilizes not only oxo formation transition states relative to the precursor M^{2+} state, but also those within the reduction half cycle in which the oxo species is consumed but that still retain bound

Table 6. Lumped kinetic parameters for MIL-100(Cr) estimated from fitting steady-state reaction data to the simplified rate expression (equation 6.10) for samples pretreated under various conditions. (Reaction at 175 °C, 2.9 – 8.7 N_2O, 3.5 – 32.2 CO).

Parameter	Equivalence	Activation Condition	Value	mol H_2O (mol Cr_3O)$^{-1}$
k_{ox}	k_2K_1	448 K, He	2.62 x 10^{-5} (kPa·s)$^{-1}$	0.61

		523 K, vacuum	1.40 x 10^{-4} (kPa·s)$^{-1}$	0.14
k_{red}	$\overrightarrow{k_3}\left(1-\frac{\overleftarrow{k_3}}{\overleftarrow{k_3}+k_4}\right)$	448 K, He	1.04 x 10^{-5} (kPa·s)$^{-1}$	0.61
		523 K, vacuum	1.98 x 10^{-5} (kPa·s)$^{-1}$	0.14

oxygen originating from the N_2O molecule. Whereas the lumped oxidation half cycle kinetic parameter k_{ox} is representative of the standard state free energy difference between the M-O bond formation transition state and the M^{2+} site (equation 6), the lumped reduction half cycle kinetic parameter k_{red} does *not* represent an analogous (but complementary) difference between the transition state for the M-O bond scission step (step 4, Scheme 1) and the metal-oxo species. It instead represents a complex combination of rate constants for steps 3 and 4 that cannot immediately be deconvoluted to obtain individual intrinsic rate constants or combinations of rate constants that represent free energy differences between specific intermediates and transition states (equation 7).

The destabilizing effect of water ligation appears to be greater on the oxidation half cycle rate constant than the reduction half cycle rate constant (Table 6), possibly due to smaller changes in oxygen coordination content expected within the reduction half cycle both due to the presence of oxygen throughout kinetically relevant transition states within exothermic reduction half cycle steps, unlike oxidation half cycle steps in which oxygen is added in to an active site that is initially devoid of oxygen. As an example, CO oxidation over $Fe_3(BTC)_2$ clusters were calculated to proceed through a 1.86 Å change in Fe-O bond lengths in the oxidation half cycle steps that were 92 kJ mol^{-1} exothermic, and reduction half cycle steps involving only a 0.05 Å change in bond length in reduction half cycle steps that were significantly more exothermic (ΔH = 278 kJ mol^{-1}).[61] The reversible but not necessarily quasiequilibrated nature of CO adsorption steps that precede highly exothermic C-O bond formation steps prevent measurement of complementary free energy differences between C-O bond formation transition states and metal-oxo species that would be expected to decrease, not increase, upon water ligation. The lumped apparent oxidation rate constant k_{ox} is more sensitive to water ligation compared to the convoluted reduction half cycle rate constant k_{red}, resulting in decreases in oxo coverages with increasing degree of hydration (Figure 14). These disproportionate changes in oxidation and reduction half cycle parameters that result in part from the exothermic nature of C-O bond formation steps render MIL-100(Cr) nodes that in their activated form have a balance of kinetic demand across the entirety of the reaction sequence to carry more of an imbalance, akin to MIL-100(Fe) nodes over which only oxidation half cycle steps that are kinetically relevant result in first and zero order behavior in N_2O and CO, respectively. Rates over the triron node, on the other hand, remain first order in N_2O regardless of degree of hydration because oxidation half cycles are disproportionately kinetically demanding on the fully thermally activated catalyst, and water ligation only serves to further accentuate this imbalance, resulting in steady state kinetic features that remain invariant in activation temperature.

The fact that hydration of nodes affects solely the rates of oxidation but not sensitivities of rates over MIL-100(Fe), but affects *both* on MIL-100(Cr) is also reflected in other kinetic features including titration transients. The use of water rather than NO as titrant results in transients in which progression of the water front through the bed causes titration of M^{2+} sites through hydroxylation, along with the concurrent hydration of Fe^{3+} sites. Normalized oxidation rates during water titrations decrease non-linearly with the cumulative moles of titrant adsorbed, consistent with the dampening of oxidation rates upon ligation of water to the secondary coordination sphere of the trimer node (Figure 15). Titrations at higher N_2O pressures (9 kPa versus 2.9 kPa), however, appear less non-linear due to the fact that hydration of Cr_3O nodes renders rates to be more sensitive to N_2O pressure such that rate differences between 2.9 and 9 kPa feeds are amplified on hydrated beds, thereby negating some of perceived non-linearity in titration data (Figure 15). MIL-100(Cr) beds appear to be more uniform at higher N_2O pressures because hydrated beds at the two different N_2O pressures are characterized by more dissimilar rates than dehydrated beds. Normalized oxidation rates on MIL-100(Fe) beds, on the other hand, also decrease non-linearly with water loading, but the degree of non-linearity tends to be independent of N_2O pressure (Figure S23, SI) owing to the fact that measured oxidation rates are dampened through hydration to the same extent regardless of the N_2O pressure under consideration. The ratio of the oxidation rate at a given water loading to that in the absence of water is determined purely by the depth of penetration of the water vapor front into the MIL-100(Fe) bed – a parameter that is clearly independent of N_2O pressure (Figure S22, SI). These titration trends help further reinforce inferences as to the disproportionate impact of second sphere water ligation on oxidation half cycles relative to reduction half cycles gleaned more directly from changes in steady state kinetic features as a function of activation temperature (Figure 14).

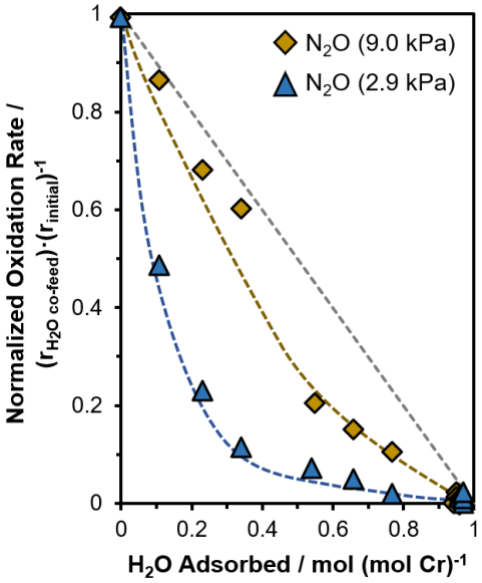

Figure 15. CO oxidation rate over MIL-100(Cr) (normalized by the oxidation rate in the absence of H_2O co-feed) as a function of the total quantity of H_2O adsorbed when H_2O (3.77 x 10^{-4} mol (mol Cr)$^{-1}$ s^{-1}) is introduced during reaction (Reaction conditions: 473 K, 9.0 or 2.9 kPa N_2O, 32 kPa CO, MIL-100(Cr) activated at 523 K under vacuum).

4. Conclusions

The two-electron oxidation of CO with N_2O over MIL-100(M) MOFs proceeds through a sequential mechanism comprised of separate oxidation and reduction half cycle steps conjoined by an active oxygen intermediate. Partially activated MIL-100(Fe) samples exhibit a distribution in active site properties, unlike fully activated ones that appear catalytically uniform. Water ligation was found to have a significant impact on the catalytic properties of these timer nodes, with turnover rates of fully hydrated samples being an order of magnitude lower than those on fully dehydrated ones. DFT analysis of reaction energetics combined with experimentally measured kinetic parameters indicate that the reduction in rates is associated with a destabilization of oxo-formation transition states relative to the Fe^{2+} precursor state, and that communication between bound water and the active site occurs through the μ_3-oxygen junction that exhibits spin density variations. In-situ infrared spectroscopy measurements indicate that water ligation results in a blueshift of the Fe^{2+}-nitrosyl band, and renders adsorption of the titrant NO at 423 K to be significantly more reversible. Partitioning the sites into those that bind NO reversibly versus irreversibly help deconvolute individual rate contributions of Fe^{2+} sites on nodes carrying three distinct degrees of hydration. Second sphere effects in which ligation away from the primary active site alters reaction energies in the absence of direct binding interactions are extended to the Cr isostructure of MIL-100(M), in which case oxidation half cycle steps involving M-O bond formation are affected disproportionately compared to reduction half cycles comprising M-O bond scission steps. This disparity in second sphere perturbation enables a kinetic mimicking of the MIL-100(Fe) sample by constraining through ligation the oxidation half cycle on the MIL-100(Cr) more so than the reduction half cycle. The extent of second sphere perturbation can be controlled by varying oxygenate identity, pointing both to the generality of these perturbative effects as well as the availability of a larger palette of synthetic levers than previously envisioned. Lastly, MOFs serve as a platform for elucidating, with clarity, catalytic phenomena that would otherwise remain recalcitrant to quantitative kinetic inquiry.

ASSOCIATED CONTENT

Supporting Information

The Supporting Information is available free of charge on the ACS Publications website.

Details of computational methods and supplementary results, supporting oxidation reaction kinetic results, XAFS results, IR spectroscopy results, additional titration results (PDF)

AUTHOR INFORMATION

Corresponding Author

* Praveen Bollini - William A. Brookshire Department of Chemical and Biomolecular Engineering; University of Houston; Houston, TX 77204, USA; Email: ppbollin@uh.edu

Present Addresses

†Chemical Sciences and Engineering Division, Argonne National Laboratory, Lemont, IL 60439, USA

Author Contributions

Conceptualization, writing and editing: PB; experiments and analysis, writing and editing: JNH; computational analysis and writing: SPV; XAFS experiments and analysis, review and editing: AJK; XAFS analysis, review and editing: MD.

ACKNOWLEDGMENT

JNH and PB acknowledge funding resources through award # 61226-DNI5 from the American Chemical Society Petroleum Research Fund. A portion of this material is based upon work supported by the U.S. Department of Energy, Office of Science, Office of Workforce Development for Teachers and Scientists, Office of Science Graduate Student Research (SCGSR) program. The SCGSR program is administered by the Oak Ridge Institute for Science and Education (ORISE) for the DOE. ORISE is managed by ORAU under contract number DE-SC0014664. All opinions expressed in this paper are the author's and do not necessarily reflect the policies and views of DOE, ORAU, or ORISE. JNH, AJK, and MD acknowledge that work at Argonne National Laboratory was supported by the U.S. Department of Energy (DOE), Office of Basic Energy Sciences, Division of Chemical Sciences, Geosciences, and Biosciences, Catalysis Science Program under Contract No. DE-AC-02-06CH11357. Use of the Advanced Photon Source is supported by the U.S. Department of Energy, Office of Science, and Office of Basic Energy Sciences, under

Contract No. DEAC02−06CH11357. MRCAT operations at Sector 10 are supported by the Department of Energy and the MRCAT member institutions. SPV appreciates Clemson's Center for Optical Materials Science and Engineering Technologies (COMSET) for funding through NSF DMR # 1950557. SPV acknowledges the Clemson Computing and Information Technology (CITI) Research Computing and Data (RCD) group for the generous allotment of compute time on the Palmetto cluster. SPV thanks Dr. Rachel B. Getman (Ohio State University) and Dr. Jenny G. Vitillo (University of Insubria, Italy) for insightful modeling conversations.

REFERENCES

(1) Poznansky, M. J.; Singh, R.; Singh, B. Current Ideas on the Chemical Mechanism of Ribonucleotide Reductase. *Drug Deliv.* **1982**, *57*, 301–329.

(2) Kauzlarich, S. M.; Teo, B. K.; Zirinc, T.; Burman, S.; Davis, J. C.; Averill, B. A. X-Ray Absorption Studies of the Purple Acid Phosphatase from Beef Spleen. *Inorg. Chem.* **1986**, *25*, 2781–2785.

(3) Rosenzweig, A. C.; Lippard, S. J. Determining the Structure of a Hydroxylase Enzyme That Catalyzes the Conversion of Methane to Methanol in Methanotrophic Bacteria. *Acc. Chem. Res.* **1994**, *27*, 229–236.

(4) Do, L. H.; Lippard, S. J. Evolution of Strategies to Prepare Synthetic Mimics of Carboxylate-Bridged Diiron Protein Active Sites. *J. Inorg. Biochem.* **2011**, *105*, 1774–1785.

(5) Zecchina, A.; Rivallan, M.; Berlier, G.; Lamberti, C.; Ricchiardi, G. Structure and Nuclearity of Active Sites in Fe-Zeolites: Comparison with Iron Sites in Enzymes and Homogeneous Catalysts. *Physical Chemistry Chemical Physics*. The Royal Society of Chemistry July 5, 2007, pp 3483–3499.

(6) Pérez-Mayoral, E.; Čejka, J. [Cu3(BTC)2]: A Metal-Organic Framework Catalyst for the Friedländer Reaction. *ChemCatChem* **2011**, *3*, 157–159.

(7) Vimont, A.; Goupil, J.-M.; Lavalley, J.-C.; Daturi, M.; Surblé, S.; Serre, C.; Millange, F.; Fé, G.; Audebrand, N. Investigation of Acid Sites in a Zeotypic Giant Pores Chromium(III) Carboxylate. *J. Am. Chem. Soc.* **2006**, *128*, 3218–3227.

(8) Yoon, J. W.; Chang, H.; Lee, S.-J.; Hwang, Y. K.; Hong, D.-Y.; Lee, S.-K.; Lee, J. S.; Jang, S.; Yoon, T.-U.; Kwac, K.; Jung, Y.; Pillai, R. S.; Faucher, F.; Vimont, A.; Daturi, M.; Férey, G.; Serre, C.; Maurin, G.; Bae, Y.-S.; Chang, J.-S. Selective Nitrogen Capture by Porous Hybrid Materials Containing Accessible Transition Metal Ion Sites. *Nat. Mater.* **2017**, *16*, 526–531.

(9) Bollini, P.; Hall, J. Quantification of Open-Metal Sites in Metal-Organic Frameworks Using Irreversible Water Adsorption. *Langmuir* **2020**, acs.langmuir.9b03581.

(10) Hall, J. N.; Bollini, P. Low-Temperature, Ambient Pressure Oxidation of Methane to Methanol Over Every Tri-Iron Node in a Metal–Organic Framework Material. *Chem. – A Eur. J.* **2020**, *26*, 16639–16643.

(11) Hall, J. N.; Bollini, P. Role of Metal Identity and Speciation in the Low-Temperature Oxidation of Methane over Tri-Metal Oxo Clusters. *AIChE J.* **2021**, *67*, e17496.

(12) Yuan, S.; Feng, L.; Wang, K.; Pang, J.; Bosch, M.; Lollar, C.; Sun, Y.; Qin, J.; Yang, X.; Zhang, P.; Wang, Q.; Zou, L.; Zhang, Y.; Zhang, L.; Fang, Y.; Li, J.; Zhou, H.-C. Stable Metal–Organic Frameworks: Design, Synthesis, and Applications. *Adv. Mater.* **2018**, *30*, 1704303.

(13) Cannon, R. D.; White, R. P. Cannon - Inorganic Chem. *Prog. Inorg. Chem.* **1988**, *36*, 195–298.

(14) C. E. Anson; J. P. Bourke; R. D. Cannon, *; U. A. Jayasooriya; M. Molinier, and; Powell, A. K. Crystal Structures of the Isomorphous Prototypic Oxo-Centered Trinuclear Complexes [Cr3O(OOCCH3)6(H2O)3]Cl·6H2O and [Fe3O(OOCCH3)6(H2O)3]Cl·6H2O. *Inorg. Chem.* **1997**, *36*, 1265–1267.

(15) Uemura, S.; Spencer, A.; Wilkinson, G. M3-Oxotrimetal Acetato-Complexes of Chromium, Manganese, Iron, Cobalt, Rhodium, and Iridium. *J. Chem. Soc. Dalt. Trans.* **1973**, No. 23, 2565–2571.

(16) Blake, A. B.; Yavari, A.; Hatfield, W. E.; Sethulekshmi, C. N. Magnetic and Spectroscopic Properties of Some Heterotrinuclear Basic Acetates of Chromium(III), Iron(III), and Divalent Metal Ions. *J. Chem. Soc. Dalt. Trans.* **1985**, No. 12, 2509–2520.

(17) Belmore, K.; Madison, X. J.; Harton, A.; Vincent, J. B. Carbon-13 NMR Studies of Oxo-Centered Trinuclear Chromium(III) Complexes of the General Formula [Cr3O(O2CR)6(L)3]+ (R = Me, Ph; L = H2O, Py). *Spectrochim. Acta Part A Mol. Spectrosc.* **1994**, *50*, 2365–2370.

(18) Blake, A. B.; Sinn, E.; Yavari, A.; Murray, K. S.; Moubaraki, B. Oxo-Centred Trinuclear Acetate Complexes Containing Mixed-Metal Clusters. Crystal Structure of a Chromium(III)Iron(III)Nickel(II) Complex and Magnetic Properties of a Dichromium(III)Magnesium(II) Complex. *Dalt. Trans.* **1998**, *1*, 45–50.

(19) Lang, J.; Hewer, J. M.; Meyer, J.; Schuchmann, J.; Van Wüllen, C.; Niedner-Schatteburg, G. Magnetostructural Correlation in Isolated Trinuclear Iron(III) Oxo Acetate Complexes. *Phys. Chem. Chem. Phys.* **2018**, *20*, 16673–16685.

(20) Baumann, J. A.; Salmon, D. J.; Wilson, S. T.; Meyer, T. J.; Hatfield, W. E. Electronic Structure and Redox Properties of the Clusters [Ru3O(CH3CO2)6L3]N+. *Inorg. Chem.* **1978**, *17*, 3342–3350.

(21) Jang, H. G.; Geib, S. J.; Kaneko, Y.; Nakano, M.; Sorai, M.; Rheingold, A. L.; Montez, B.; Hendrickson, D. N. Lattice-Engineered Micromodulation of Intramolecular Electron-Transfer Rates in Trinuclear Mixed-Valence Iron Acetate Complexes. *J. Am. Chem. Soc.* **1989**, *111*, 173–186.

(22) Wu, R.; Poyraz, M.; Sowrey, F. E.; Anson, C. E.; Wocadlo, S.; Powell, A. K.; Jayasooriya, U. A.; Cannon, R. D.; Nakamoto, T.; Katada, M.; Sano, H. Electron Localization and Delocalization in Mixed-Valence Transition Metal Clusters: Structural and Spectroscopic Studies of Oxo-Centered Trinuclear Complexes [Fe3O(OOCCMe3)6(Py)3]+/0 and [Mn3O(OOCCMe3)6(Py)3]+/0. *Inorg. Chem.* **1998**, *37*, 1913–1921.

(23) Stadler, C.; Daub, J.; KÃ¶hler, J.; Saalfrank, R. W.; Coropceanu, V.; SchÃ¼nemann, V.; Ober, C.; Trautwein, A. X.; Parker, S. F.; Poyraz, M.; Inomata, T.; Cannon, R. D. Electron Transfer in a Trinuclear Oxo-Centred Mixed-Valence Iron Complex, in Solid and Solution States. *J. Chem. Soc. Dalt. Trans.* **2001**, No. 22, 3373–3383.

(24) Overgaard, J.; Larsen, F. K.; Schiøtt, B.; Iversen, B. B. Electron Density Distributions of Redox Active Mixed Valence Carboxylate Bridged Trinuclear Iron Complexes. *J. Am. Chem. Soc.* **2003**, *125*, 11088–11099.

(25) Harton, A.; Nagi, M. K.; Glass, M. M.; Junk, P. C.; Atwood, J. L.; Vincent, J. B. Synthesis and Characterization of Symmetric and Unsymmetric Oxo-Bridged Trinuclear Chromium Benzoate Complexes: Crystal and Molecular Structure of [Cr3O(O2CPh)6(Py)3]ClO4. *Inorganica Chim. Acta* **1994**, *217*, 171–179.

(26) Kou, N.; Tadashi, Y.; Yoichi, S.; Tasuku, I. Synthesis of Trinuclear Molybdenum Cluster Complex with Novel Skeleton, [Mo3(M3-CCH3)(M3-O)(μ-C6H5COO)6(CH3OH)3]Cl through Bridging Carboxylate Ligand Substitution. *Chem. Lett.* **1992**, *21*, 983–986.

(27) Ito, S.; Inoue, K.; Mastumoto, M. [Fe3O(OCOR)6L3]+-Catalyzed Epoxidation of Olefinic Alcohol Acetates by Molecular

Oxygen. *J. Am. Chem. Soc.* **1982**, *104*, 6450–6452.

(28) Fouda, S. A.; Rempel, G. L. M3-Oxo-Triruthenium Acetate Cluster Complexes as Catalysts for Olefin Hydrogenation. *Inorg. Chem.* **1979**, *18*, 1–8.

(29) Nunes, G. S.; Alexiou, A. D. P.; Toma, H. E. Catalytic Oxidation of Hydrocarbons by Trinuclear μ-Oxo-Bridged Ruthenium-Acetate Clusters: Radical versus Non-Radical Mechanisms. *J. Catal.* **2008**, *260*, 188–192.

(30) Bhunia, S.; Ghatak, A.; Dey, A. Second Sphere Effects on Oxygen Reduction and Peroxide Activation by Mononuclear Iron Porphyrins and Related Systems. *Chem. Rev.* **2022**, *122*, 12370–12426.

(31) Rhoda, H. M.; Heyer, A. J.; Snyder, B. E. R.; Plessers, D.; Bols, M. L.; Schoonheydt, R. A.; Sels, B. F.; Solomon, E. I. Second-Sphere Lattice Effects in Copper and Iron Zeolite Catalysis. *Chem. Rev.* **2022**, *122*, 12207–12243.

(32) Leenders, S. H. A. M.; Gramage-Doria, R.; De Bruin, B.; Reek, J. N. H. Transition Metal Catalysis in Confined Spaces. *Chem. Soc. Rev.* **2014**, *44*, 433–448.

(33) Singha, A.; Dey, A. Hydrogen Atom Abstraction by Synthetic Heme Ferric Superoxide and Hydroperoxide Species. *Chem. Commun.* **2019**, *55*, 5591–5594.

(34) Hall, J. N.; Kropf, A. J.; Delferro, M.; Bollini, P. Kinetic and X-Ray Absorption Spectroscopic Analysis of Catalytic Redox Cycles over Highly Uniform Polymetal Oxo Clusters. *ACS Catal.* **2023**, *13*, 5406–5427.

(35) Kraft, S.; Stümpel, J.; Becker, P.; Kuetgens, U. High Resolution X-ray Absorption Spectroscopy with Absolute Energy Calibration for the Determination of Absorption Edge Energies. *Rev. Sci. Instrum.* **1998**, *67*, 681.

(36) Ravel, B.; Newville, M. ATHENA, ARTEMIS, HEPHAESTUS: Data Analysis for X-Ray Absorption Spectroscopy Using IFEFFIT. *J. Synchrotron Rad.* **2005**, *12*, 537–541.

(37) Horcajada, P.; Surblé, S.; Serre, C.; Hong, D. Y.; Seo, Y. K.; Chang, J. S.; Grenèche, J. M.; Margiolaki, I.; Férey, G. Synthesis and Catalytic Properties of MIL-100(Fe), an Iron(III) Carboxylate with Large Pores. *Chem. Commun.* **2007**, *100*, 2820–2822.

(38) Zabinsky, S. I.; Rehr, J. J.; Ankudinov, A.; Albers, R. C.; Eller, M. J. Multiple-Scattering Calculations of x-Ray-Absorption Spectra. *Phys. Rev. B* **1995**, *52*, 2995.

(39) Zhao, Y.; Truhlar, D. G. The M06 Suite of Density Functionals for Main Group Thermochemistry, Thermochemical Kinetics, Noncovalent Interactions, Excited States, and Transition Elements: Two New Functionals and Systematic Testing of Four M06-Class Functionals and 12 Other Functionals. *Theor. Chem. Acc.* **2008**, *120*, 215–241.

(40) Weigend, F.; Ahlrichs, R. Balanced Basis Sets of Split Valence, Triple Zeta Valence and Quadruple Zeta Valence Quality for H to Rn: Design and Assessment of Accuracy. *Phys. Chem. Chem. Phys.* **2005**, *7*, 3297–3305.

(41) Weigend, F. Accurate Coulomb-Fitting Basis Sets for H to Rn. *Phys. Chem. Chem. Phys.* **2006**, *8*, 1057–1065.

(42) Frisch, M. J.; Trucks, G. W.; Schlegel, H. B.; Scuseria, G. E.; Robb, M. A.; Cheeseman, J. R.; Scalmani, G.; Barone, V.; Petersson, G. A.; Nakatsuji, H.; Li, X.; Caricato, M.; Marenich, A. V.; Bloino, J.; Janesko, B. G.; Gomperts, R.; Mennucci, B.; Hratch, D. J. Gaussian 16, Revision C.02. Gaussian, Inc.: Wallingford, CT 2019.

(43) Vitillo, J. G.; Bhan, A.; Cramer, C. J.; Lu, C. C.; Gagliardi, L. Quantum Chemical Characterization of Structural Single Fe(II) Sites in MIL-Type Metal–Organic Frameworks for the Oxidation of Methane to Methanol and Ethane to Ethanol. *ACS Catal.* **2019**, *9*, 2870–2879.

(44) Vitillo, J. G.; Gagliardi, L. Thermal Treatment Effect on CO and NO Adsorption on Fe(II) and Fe(III) Species in Fe3O-Based MIL-Type Metal-Organic Frameworks: A Density Functional Theory Study. *Inorg. Chem.* **2021**, *60*, 11813–11824.

(45) Vitillo, J. G.; Lu, C. C.; Cramer, C. J.; Bhan, A.; Gagliardi, L. Influence of First and Second Coordination Environment on Structural Fe(II) Sites in MIL-101 for C-H Bond Activation in Methane. *ACS Catal.* **2021**, *11*, 579–589.

(46) GitHub - getman-research-group/MIL-100-Second-Sphere-Coordination-Effects https://github.com/getman-research-group/MIL-100-Second-Sphere-Coordination-Effects/ (accessed 2023 -09 -26).

(47) Shabbir, H.; Pellizzeri, S.; Ferrandon, M.; Kim, I. S.; Vermeulen, N. A.; Farha, O. K.; Delferro, M.; Martinson, A. B. F.; Getman, R. B. Influence of Spin State and Electron Configuration on the Active Site and Mechanism for Catalytic Hydrogenation on Metal Cation Catalysts Supported on NU-1000: Insights from Experiments and Microkinetic Modeling. *Catal. Sci. Technol.* **2020**, *10*, 3594–3602.

(48) Lym, J.; Wittreich, G. R.; Vlachos, D. G. A Python Multiscale Thermochemistry Toolbox (PMuTT) for Thermochemical and Kinetic Parameter Estimation. *Comput. Phys. Commun.* **2020**, *247*, 106864.

(49) Yoon, J. W.; Seo, Y.-K.; Hwang, Y. K.; Chang, J.-S.; Leclerc, H.; Wuttke, S.; Bazin, P.; Vimont, A.; Daturi, M.; Bloch, E.; Llewellyn, P. L.; Serre, C.; Horcajada, P.; Grenèche, J.-M.; Rodrigues, A. E.; Férey, G. Controlled Reducibility of a Metal-Organic Framework with Coordinatively Unsaturated Sites for Preferential Gas Sorption. *Angew. Chem. Int. Ed.* **2010**, *49*, 5949–5952.

(50) Sudik, A. C.; Cô Té, A. P.; Yaghi, O. M. Metal-Organic Frameworks Based on Trigonal Prismatic Building Blocks and the New "Acs" Topology. *Inorg. Chem.* **2005**, *44*, 2998–3000.

(51) Simons, M. C.; Vitillo, J. G.; Babucci, M.; Hoffman, A. S.; Boubnov, A.; Beauvais, M. L.; Chen, Z.; Cramer, C. J.; Chapman, K. W.; Bare, S. R.; Gates, B. C.; Lu, C. C.; Gagliardi, L.; Bhan, A. Structure, Dynamics, and Reactivity for Light Alkane Oxidation of Fe(II) Sites Situated in the Nodes of a Metal–Organic Framework. *J. Am. Chem. Soc.* **2019**, *141*, 18142–18151.

(52) Westre, T. E.; Kennepohl, P.; DeWitt, J. G.; Hedman, B.; Hodgson, K. O.; Solomon, E. I. A Multiplet Analysis of Fe K-Edge 1s → 3d Pre-Edge Features of Iron Complexes. *J. Am. Chem. Soc.* **1997**, *119*, 6297–6314.

(53) Vogel, K. M.; Kozlowski, P. M.; Zgierski, M. Z.; Spiro, T. G. Determinants of the FeXO (X = C, N, O) Vibrational Frequencies in Heme Adducts from Experiment and Density Functional Theory. *J. Am. Chem. Soc.* **1999**, *121*, 9915–9921.

(54) Peri, J. B. Infrared Study of Nitric Oxide and Carbon Monoxide Adsorbed on Chromia/Alumina. *J. Phys. Chem.* **1974**, *78*, 588–594.

(55) Spiro, T. G.; Soldatova, A. V.; Balakrishnan, G. CO, NO and O2 as Vibrational Probes of Heme Protein Interactions. *Coord. Chem. Rev.* **2013**, *257*, 511.

(56) Goodrich, L. E.; Paulat, F.; Praneeth, V. K. K.; Lehnert, N. Electronic Structure of Heme-Nitrosyls and Its Significance for Nitric Oxide Reactivity, Sensing, Transport, and Toxicity in Biological Systems. *Inorg. Chem.* **2010**, *49*, 6293–6316.

(57) Wuttke, S.; Bazin, P.; Vimont, A.; Serre, C.; Seo, Y. K.; Hwang, Y. K.; Chang, J. S.; Férey, G.; Daturi, M. Discovering the Active Sites for C3 Separation in MIL-100(Fe) by Using Operando IR Spectroscopy. *Chem. - A Eur. J.* **2012**, *18*, 11959–11967.

(58) Eubank, J. F.; Wheatley, P. S.; Lebars, G.; McKinlay, A. C.; Leclerc, H.; Horcajada, P.; Daturi, M.; Vimont, A.; Morris, R. E.; Serre, C. Porous, Rigid Metal(III)-Carboxylate Metal-Organic Frameworks for the Delivery of Nitric Oxide. *APL Mater.* **2014**, *2*, 124112–1.

(59) Leclerc, H.; Vimont, A.; Lavalley, J. C.; Daturi, M.; Wiersum, A. D.; Llwellyn, P. L.; Horcajada, P.; Férey, G.; Serre, C. Infrared Study of the Influence of Reducible Iron(III) Metal Sites on the Adsorption of CO, CO2, Propane, Propene and Propyne in the Mesoporous Metalorganic Framework MIL-100. *Phys. Chem. Chem. Phys.* **2011**, *13*, 11748–11756.

(60) Rivallan, M.; Bromley, B.; Kiwi-Minsker, L. Do Synthetic Fe-Zeolites Mimic Biological Fe-Porphyrins in Reactions with Nitric Oxide? *Catal. Today* **2010**, *157*, 223–230.

(61) Ketrat, S.; Maihom, T.; Wannakao, S.; Probst, M.; Nokbin, S.; Limtrakul, J. Coordinatively Unsaturated Metal-Organic Frameworks M3(Btc)2 (M = Cr, Fe, Co, Ni, Cu, and Zn) Catalyzing the Oxidation of CO by N2O: Insight from DFT Calculations. *Inorg. Chem.* **2017**, *56*, 14005–14012.

.

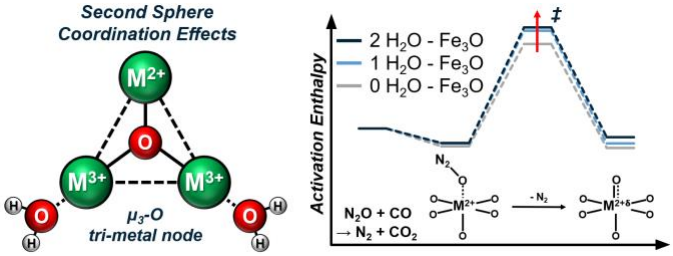
Second Sphere
Coordination Effects
M2+
O
M3+
M3+
O
O
H
H
H
H
μ3-O
tri-metal node
Activation Enthalpy
2 H2O - Fe3O
1 H2O - Fe3O
0 H2O - Fe3O
‡
N2
- N2
N2O + CO
→ N2 + CO2